

Clouds and the Earth's Radiant Energy System (CERES) Algorithm Theoretical Basis Document

Volume III—Cloud Analyses and Determination of Improved Top of Atmosphere Fluxes (Subsystem 4)

*CERES Science Team
Langley Research Center • Hampton, Virginia*

Available electronically at the following URL address: <http://techreports.larc.nasa.gov/ltrs/ltrs.html>

Printed copies available from the following:

NASA Center for AeroSpace Information
800 Elkridge Landing Road
Linthicum Heights, MD 21090-2934
(301) 621-0390

National Technical Information Service (NTIS)
5285 Port Royal Road
Springfield, VA 22161-2171
(703) 487-4650

Contents

Preface v

Nomenclatureix

CERES Top Level Data Flow Diagram xvii

Subsystem 4.0 Top Level Data Flow Diagram xviii

Overview of Cloud Retrieval and Radiative Flux Inversion (Subsystem (4.0) 1

Imager Clear-Sky Determination and Cloud Detection (Subsystem 4.1) 43

Imager Cloud Height Determination (Subsystem 4.2)..... 83

Cloud Optical Property Retrieval (Subsystem 4.3) 135

Convolution of Imager Cloud Properties With CERES Footprint Point Spread Function
(Subsystem 4.4)..... 177

CERES Inversion to Instantaneous TOA Fluxes (Subsystem 4.5)..... 195

Empirical Estimates of Shortwave and Longwave Surface Radiation Budget Involving
CERES Measurements (Subsystem 4.6.0) 207

Estimate of Shortwave Surface Radiation Budget From CERES (Subsystem 4.6.1) 213

Estimation of Longwave Surface Radiation Budget From CERES (Subsystem 4.6.2)..... 217

An Algorithm for Longwave Surface Radiation Budget for Total Skies (Subsystem 4.6.3)..... 235

Preface

The Release-1 CERES Algorithm Theoretical Basis Document (ATBD) is a compilation of the techniques and processes that constitute the prototype data analysis scheme for the Clouds and the Earth's Radiant Energy System (CERES), a key component of NASA's Mission to Planet Earth. The scientific bases for this project and the methodologies used in the data analysis system are also explained in the ATBD. The CERES ATBD comprises 11 subsystems of various sizes and complexities. The ATBD for each subsystem has been reviewed by three or four independently selected university, NASA, and NOAA scientists. In addition to the written reviews, each subsystem ATBD was reviewed during oral presentations given to a six-member scientific peer review panel at Goddard Space Flight Center during May 1994. Both sets of reviews, oral and written, determined that the CERES ATBD was sufficiently mature for use in providing archived Earth Observing System (EOS) data products. The CERES Science Team completed revisions of the ATBD to satisfy all reviewer comments. Because the Release-1 CERES ATBD will serve as the reference for all of the initial CERES data analysis algorithms and product generation, it is published here as a NASA Reference Publication.

Due to its extreme length, this NASA Reference Publication comprises four volumes that divide the CERES ATBD at natural break points between particular subsystems. These four volumes are

- I: Overviews
 - CERES Algorithm Overview
 - Subsystem 0. CERES Data Processing System Objectives and Architecture
- II: Geolocation, Calibration, and ERBE-Like Analyses
 - Subsystem 1.0. Instrument Geolocate and Calibrate Earth Radiances
 - Subsystem 2.0. ERBE-Like Inversion to Instantaneous TOA and Surface Fluxes
 - Subsystem 3.0. ERBE-Like Averaging to Monthly TOA
- III: Cloud Analyses and Determination of Improved Top of Atmosphere Fluxes
 - Subsystem 4.0. Overview of Cloud Retrieval and Radiative Flux Inversion
 - Subsystem 4.1. Imager Clear-Sky Determination and Cloud Detection
 - Subsystem 4.2. Imager Cloud Height Determination
 - Subsystem 4.3. Cloud Optical Property Retrieval
 - Subsystem 4.4. Convolution of Imager Cloud Properties With CERES Footprint Point Spread Function
 - Subsystem 4.5. CERES Inversion to Instantaneous TOA Fluxes
 - Subsystem 4.6. Empirical Estimates of Shortwave and Longwave Surface Radiation Budget Involving CERES Measurements
- IV: Determination of Surface and Atmosphere Fluxes and Temporally and Spatially Averaged Products
 - Subsystem 5.0. Compute Surface and Atmospheric Fluxes
 - Subsystem 6.0. Grid Single Satellite Fluxes and Clouds and Compute Spatial Averages
 - Subsystem 7.0. Time Interpolation and Synoptic Flux Computation for Single and Multiple Satellites
 - Subsystem 8.0. Monthly Regional, Zonal, and Global Radiation Fluxes and Cloud Properties
 - Subsystem 9.0. Grid TOA and Surface Fluxes for Instantaneous Surface Product
 - Subsystem 10.0. Monthly Regional TOA and Surface Radiation Budget
 - Subsystem 11.0. Update Clear Reflectance, Temperature History (CHR)
 - Subsystem 12.0. Regrid Humidity and Temperature Fields

The CERES Science Team serves as the editor for the entire document. A complete list of Science Team members is given below. Different groups of individuals prepared the various subsections that constitute the CERES ATBD. Thus, references to a particular subsection of the ATBD should specify

the subsection number, authors, and page numbers. Questions regarding the content of a given subsection should be directed to the appropriate first or second author. No attempt was made to make the overall document stylistically consistent.

The CERES Science Team is an international group led by 2 principal investigators and 19 coinvestigators. The team members and their institutions are listed below.

CERES Science Team

Bruce A. Wielicki, Interdisciplinary Principal Investigator
Bruce R. Barkstrom, Instrument Principal Investigator

Atmospheric Sciences Division
NASA Langley Research Center
Hampton, Virginia 23681-0001

Coinvestigators

Bryan A. Baum
Atmospheric Sciences Division
NASA Langley Research Center
Hampton, Virginia 23681-0001

Maurice Blackmon
Climate Research Division
NOAA Research Laboratory
Boulder, Colorado 80303

Robert D. Cess
Institute for Terrestrial & Planetary Atmospheres
Marine Sciences Research Center
State University of New York
Stony Brook, New York 11794-5000

Thomas P. Charlock
Atmospheric Sciences Division
NASA Langley Research Division
Hampton, Virginia 23681-0001

James A. Coakley
Oregon State University
Department of Atmospheric Sciences
Corvallis, Oregon 97331-2209

Dominique A. Crommelynck
Institute Royal Meteorologique
B-1180 Bruxelles
Belgium

Richard N. Green
Atmospheric Sciences Division
NASA Langley Research Center
Hampton, Virginia 23681-0001

Robert Kandel
Laboratoire de Meteorologie Dynamique
Ecole Polytechnique
91128 Palaiseau
France

Michael D. King
Goddard Space Flight Center
Greenbelt, Maryland 20771

Robert B. Lee III
Atmospheric Sciences Division
NASA Langley Research Center
Hampton, Virginia 23681-0001

A. James Miller
NOAA/NWS
5200 Auth Road
Camp Springs, Maryland 20233

Patrick Minnis
Atmospheric Sciences Division
NASA Langley Research Center
Hampton, Virginia 23681-0001

Veerabhadran Ramanathan
Scripps Institution of Oceanography
University of California-San Diego
La Jolla, California 92093-0239

David R. Randall
Colorado State University
Department of Atmospheric Science
Foothills Campus, Laporte Avenue
Fort Collins, Colorado 80523

G. Louis Smith
Atmospheric Sciences Division
NASA Langley Research Center
Hampton, Virginia 23681-0001

Larry L. Stowe
NOAA/NWS
5200 Auth Road
Camp Springs, Maryland 20233

Ronald M. Welch
South Dakota School of Mines and Technology
Institute of Atmospheric Sciences
Rapid City, South Dakota 57701-3995

Nomenclature

Acronyms

ADEOS	Advanced Earth Observing System
ADM	Angular Distribution Model
AIRS	Atmospheric Infrared Sounder (EOS-AM)
AMSU	Advanced Microwave Sounding Unit (EOS-PM)
APD	Aerosol Profile Data
APID	Application Identifier
ARESE	ARM Enhanced Shortwave Experiment
ARM	Atmospheric Radiation Measurement
ASOS	Automated Surface Observing Sites
ASTER	Advanced Spaceborne Thermal Emission and Reflection Radiometer
ASTEX	Atlantic Stratocumulus Transition Experiment
ASTR	Atmospheric Structures
ATBD	Algorithm Theoretical Basis Document
AVG	Monthly Regional, Average Radiative Fluxes and Clouds (CERES Archival Data Product)
AVHRR	Advanced Very High Resolution Radiometer
BDS	Bidirectional Scan (CERES Archival Data Product)
BRIE	Best Regional Integral Estimate
BSRN	Baseline Surface Radiation Network
BTD	Brightness Temperature Difference(s)
CCD	Charge Coupled Device
CCSDS	Consultative Committee for Space Data Systems
CEPEX	Central Equatorial Pacific Experiment
CERES	Clouds and the Earth's Radiant Energy System
CID	Cloud Imager Data
CLAVR	Clouds from AVHRR
CLS	Constrained Least Squares
COPRS	Cloud Optical Property Retrieval System
CPR	Cloud Profiling Radar
CRH	Clear Reflectance, Temperature History (CERES Archival Data Product)
CRS	Single Satellite CERES Footprint, Radiative Fluxes and Clouds (CERES Archival Data Product)
DAAC	Distributed Active Archive Center
DAC	Digital-Analog Converter
DB	Database
DFD	Data Flow Diagram
DLF	Downward Longwave Flux

DMSP	Defense Meteorological Satellite Program
EADM	ERBE-Like Albedo Directional Model (CERES Input Data Product)
ECA	Earth Central Angle
ECLIPS	Experimental Cloud Lidar Pilot Study
ECMWF	European Centre for Medium-Range Weather Forecasts
EDDB	ERBE-Like Daily Data Base (CERES Archival Data Product)
EID9	ERBE-Like Internal Data Product 9 (CERES Internal Data Product)
EOS	Earth Observing System
EOSDIS	Earth Observing System Data Information System
EOS-AM	EOS Morning Crossing Mission
EOS-PM	EOS Afternoon Crossing Mission
ENSO	El Niño/Southern Oscillation
ENVISAT	Environmental Satellite
EPHANC	Ephemeris and Ancillary (CERES Input Data Product)
ERB	Earth Radiation Budget
ERBE	Earth Radiation Budget Experiment
ERBS	Earth Radiation Budget Satellite
ESA	European Space Agency
ES4	ERBE-Like S4 Data Product (CERES Archival Data Product)
ES4G	ERBE-Like S4G Data Product (CERES Archival Data Product)
ES8	ERBE-Like S8 Data Product (CERES Archival Data Product)
ES9	ERBE-Like S9 Data Product (CERES Archival Data Product)
FLOP	Floating Point Operation
FIRE	First ISCCP Regional Experiment
FIRE II IFO	First ISCCP Regional Experiment II Intensive Field Observations
FOV	Field of View
FSW	Hourly Gridded Single Satellite Fluxes and Clouds (CERES Archival Data Product)
FTM	Functional Test Model
GAC	Global Area Coverage (AVHRR data mode)
GAP	Gridded Atmospheric Product (CERES Input Data Product)
GCIP	GEWEX Continental-Phase International Project
GCM	General Circulation Model
GEBA	Global Energy Balance Archive
GEO	ISSCP Radiances (CERES Input Data Product)
GEWEX	Global Energy and Water Cycle Experiment
GLAS	Geoscience Laser Altimetry System
GMS	Geostationary Meteorological Satellite
GOES	Geostationary Operational Environmental Satellite
HBTM	Hybrid Bispectral Threshold Method

HIRS	High-Resolution Infrared Radiation Sounder
HIS	High-Resolution Interferometer Sounder
ICM	Internal Calibration Module
ICRCCM	Intercomparison of Radiation Codes in Climate Models
ID	Identification
IEEE	Institute of Electrical and Electronics Engineers
IES	Instrument Earth Scans (CERES Internal Data Product)
IFO	Intensive Field Observation
INSAT	Indian Satellite
IOP	Intensive Observing Period
IR	Infrared
IRIS	Infrared Interferometer Spectrometer
ISCCP	International Satellite Cloud Climatology Project
ISS	Integrated Sounding System
IWP	Ice Water Path
LAC	Local Area Coverage (AVHRR data mode)
LaRC	Langley Research Center
LBC	Laser Beam Ceilometer
LBTM	Layer Bispectral Threshold Method
Lidar	Light Detection and Ranging
LITE	Lidar In-Space Technology Experiment
Lowtran 7	Low-Resolution Transmittance (Radiative Transfer Code)
LW	Longwave
LWP	Liquid Water Path
LWRE	Longwave Radiant Excitance
MAM	Mirror Attenuator Mosaic
MC	Mostly Cloudy
MCR	Microwave Cloud Radiometer
METEOSAT	Meteorological Operational Satellite (European)
METSAT	Meteorological Satellite
MFLOP	Million FLOP
MIMR	Multifrequency Imaging Microwave Radiometer
MISR	Multiangle Imaging Spectroradiometer
MLE	Maximum Likelihood Estimate
MOA	Meteorology Ozone and Aerosol
MODIS	Moderate-Resolution Imaging Spectroradiometer
MSMR	Multispectral, multiresolution
MTSA	Monthly Time and Space Averaging
MWH	Microwave Humidity

MWP	Microwave Water Path
NASA	National Aeronautics and Space Administration
NCAR	National Center for Atmospheric Research
NESDIS	National Environmental Satellite, Data, and Information Service
NIR	Near Infrared
NMC	National Meteorological Center
NOAA	National Oceanic and Atmospheric Administration
NWP	Numerical Weather Prediction
OLR	Outgoing Longwave Radiation
OPD	Ozone Profile Data (CERES Input Data Product)
OV	Overcast
PC	Partly Cloudy
POLDER	Polarization of Directionality of Earth's Reflectances
PRT	Platinum Resistance Thermometer
PSF	Point Spread Function
PW	Precipitable Water
RAPS	Rotating Azimuth Plane Scan
RPM	Radiance Pairs Method
RTM	Radiometer Test Model
SAB	Sorting by Angular Bins
SAGE	Stratospheric Aerosol and Gas Experiment
SARB	Surface and Atmospheric Radiation Budget Working Group
SDCD	Solar Distance Correction and Declination
SFC	Hourly Gridded Single Satellite TOA and Surface Fluxes (CERES Archival Data Product)
SHEBA	Surface Heat Budget in the Arctic
SPECTRE	Spectral Radiance Experiment
SRB	Surface Radiation Budget
SRBAVG	Surface Radiation Budget Average (CERES Archival Data Product)
SSF	Single Satellite CERES Footprint TOA and Surface Fluxes, Clouds
SSMI	Special Sensor Microwave Imager
SST	Sea Surface Temperature
SURFMAP	Surface Properties and Maps (CERES Input Product)
SW	Shortwave
SWICS	Shortwave Internal Calibration Source
SWRE	Shortwave Radiant Excitance
SYN	Synoptic Radiative Fluxes and Clouds (CERES Archival Data Product)
SZA	Solar Zenith Angle
THIR	Temperature/Humidity Infrared Radiometer (Nimbus)

TIROS	Television Infrared Observation Satellite
TISA	Time Interpolation and Spatial Averaging Working Group
TMI	TRMM Microwave Imager
TOA	Top of the Atmosphere
TOGA	Tropical Ocean Global Atmosphere
TOMS	Total Ozone Mapping Spectrometer
TOVS	TIROS Operational Vertical Sounder
TRMM	Tropical Rainfall Measuring Mission
TSA	Time-Space Averaging
UAV	Unmanned Aerospace Vehicle
UT	Universal Time
UTC	Universal Time Code
VAS	VISSR Atmospheric Sounder (GOES)
VIRS	Visible Infrared Scanner
VISSR	Visible and Infrared Spin Scan Radiometer
WCRP	World Climate Research Program
WG	Working Group
Win	Window
WN	Window
WMO	World Meteorological Organization
ZAVG	Monthly Zonal and Global Average Radiative Fluxes and Clouds (CERES Archival Data Product)

Symbols

A	atmospheric absorptance
$B_{\lambda}(T)$	Planck function
C	cloud fractional area coverage
CF_2Cl_2	dichlorofluorocarbon
$CFCl_3$	trichlorofluorocarbon
CH_4	methane
CO_2	carbon dioxide
D	total number of days in the month
D_e	cloud particle equivalent diameter (for ice clouds)
E_o	solar constant or solar irradiance
F	flux
f	fraction
G_a	atmospheric greenhouse effect
g	cloud asymmetry parameter
H_2O	water vapor

I	radiance
i	scene type
m_i	imaginary refractive index
\hat{N}	angular momentum vector
N_2O	nitrous oxide
O_3	ozone
P	point spread function
p	pressure
Q_a	absorption efficiency
Q_e	extinction efficiency
Q_s	scattering efficiency
R	anisotropic reflectance factor
r_E	radius of the Earth
r_e	effective cloud droplet radius (for water clouds)
r_h	column-averaged relative humidity
S_o	summed solar incident SW flux
S'_o	integrated solar incident SW flux
T	temperature
T_B	blackbody temperature
t	time or transmittance
W_{liq}	liquid water path
w	precipitable water
\hat{x}_o	satellite position at t_o
x, y, z	satellite position vector components
$\dot{x}, \dot{y}, \dot{z}$	satellite velocity vector components
z	altitude
z_{top}	altitude at top of atmosphere
α	albedo or cone angle
β	cross-scan angle
γ	Earth central angle
γ_{at}	along-track angle
γ_{ct}	cross-track angle
δ	along-scan angle
ε	emittance
Θ	colatitude of satellite
θ	viewing zenith angle
θ_o	solar zenith angle
λ	wavelength
μ	viewing zenith angle cosine

μ_o	solar zenith angle cosine
ν	wave number
ρ	bidirectional reflectance
τ	optical depth
$\tau_{aer}(p)$	spectral optical depth profiles of aerosols
$\tau_{H_2O\lambda}(p)$	spectral optical depth profiles of water vapor
$\tau_{O_3}(p)$	spectral optical depth profiles of ozone
Φ	longitude of satellite
ϕ	azimuth angle
$\tilde{\omega}_o$	single-scattering albedo

Subscripts:

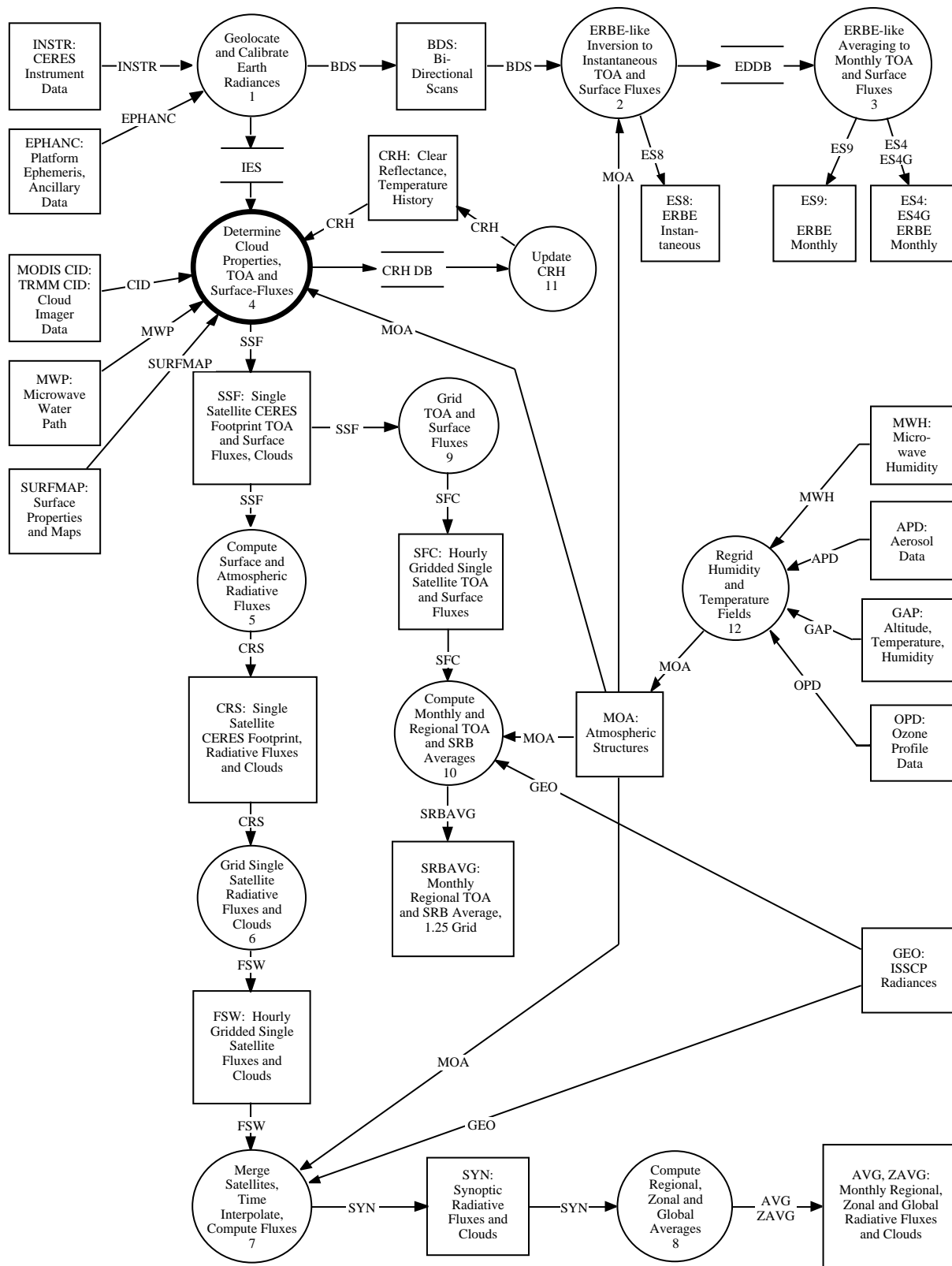
c	cloud
cb	cloud base
ce	cloud effective
cld	cloud
cs	clear sky
ct	cloud top
ice	ice water
lc	lower cloud
liq	liquid water
s	surface
uc	upper cloud
λ	spectral wavelength

Units

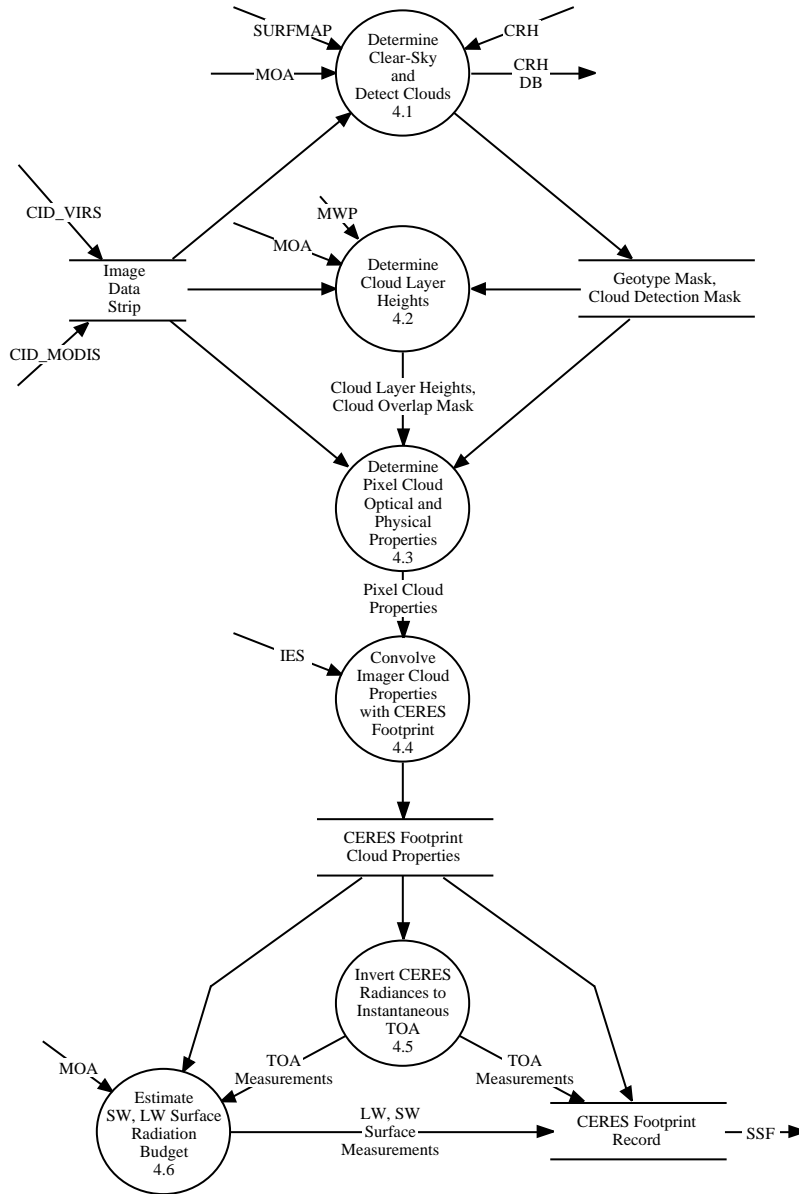
AU	astronomical unit
cm	centimeter
cm-sec ⁻¹	centimeter per second
count	count
day	day, Julian date
deg	degree
deg-sec ⁻¹	degree per second
DU	Dobson unit
erg-sec ⁻¹	erg per second
fraction	fraction (range of 0–1)
g	gram
g-cm ⁻²	gram per square centimeter
g-g ⁻¹	gram per gram
g-m ⁻²	gram per square meter

h	hour
hPa	hectopascal
K	Kelvin
kg	kilogram
kg-m ⁻²	kilogram per square meter
km	kilometer
km-sec ⁻¹	kilometer per second
m	meter
mm	millimeter
μm	micrometer, micron
N/A	not applicable, none, unitless, dimensionless
ohm-cm ⁻¹	ohm per centimeter
percent	percent (range of 0–100)
rad	radian
rad-sec ⁻¹	radian per second
sec	second
sr ⁻¹	per steradian
W	watt
W-m ⁻²	watt per square meter
W-m ⁻² sr ⁻¹	watt per square meter per steradian
W-m ⁻² sr ⁻¹ μm ⁻¹	watt per square meter per steradian per micrometer

CERES Top Level Data Flow Diagram



Subsystem 4.0 Top Level Data Flow Diagram



Clouds and the Earth's Radiant Energy System (CERES)

Algorithm Theoretical Basis Document

Cloud Optical Property Retrieval

(Subsystem 4.3)

Patrick Minnis¹

David P. Kratz¹

James A. Coakley, III²

Michael D. King³

Donald Garber⁴

Patrick Heck⁴

Shalini Mayor⁴

David F. Young⁴

Robert Arduini⁵

¹Atmospheric Sciences Division, NASA Langley Research Center, Hampton, Virginia 23681-0001

²Oregon State University, Corvallis, Oregon 97331-2209

³Goddard Space Flight Center, Greenbelt, Maryland 20771

⁴Analytical Services & Materials, Inc., Hampton, Virginia 23666

⁵Science Applications International Corporation (SAIC), Hampton, Virginia 23666

Abstract

Cloud physical and optical properties determine how clouds affect the radiance and flux fields at the surface, within the atmosphere, and at the top of the atmosphere. In this subsystem, CERES analyzes individual pixel radiances to derive the cloud properties that influence the radiation fields. For each pixel, state-of-the-art methods are used to ascertain the temperatures and pressures corresponding to the cloud top, base, and effective radiating center; the phase and effective size of the cloud particles; the cloud optical depth at a wavelength of 0.65 μm ; the cloud emittance at 10.8 μm ; and the cloud liquid or ice water path. During daytime, three different techniques will be used to account for deficiencies in any one of the individual methods. The first method uses 0.65-, 3.75-, and 10.8- μm data from VIRS, AVHRR, or MODIS data. It iteratively solves for phase, particle size, optical depth, and effective cloud temperature. Emittance is computed from the optical depth. Cloud top and base temperatures and pressures are estimated using empirical formulae based on field experiment data. The water path is computed from the particle size. The second technique uses the similarity principle with a combination of 0.65-, 1.6-, and 2.12- μm reflectance data to derive phase, particle size, and optical depth. Cloud temperature is determined by correcting the observed 10.8- μm brightness temperature for semitransparency using the retrieved optical depth. The other parameters are computed in the same manner used for the first method. This approach will be partially implemented for VIRS and AVHRR and will be fully operational for MODIS. VIRS and AVHRR lack the 2.12- μm channel that is available on MODIS. The third technique uses 3.75-, 10.8-, and 12.0- μm data to determine cloud temperature, optical depth, phase, and particle size for optically thin clouds. This last daytime method will be used mainly for shadowed clouds and thin clouds over highly reflective backgrounds. It also forms the primary method for nighttime analyses. A second nighttime analysis is used for estimating an effective size and temperature for pixel clusters. Optical depth and cloud fraction are computed for individual pixels. All of the methods currently in development will become operational for application to CERES/TRMM. Results of this subsystem will be validated using coincident datasets from field programs. The required correlative data for validation include surface and aircraft measurements of the subsystem parameters using lidars, radars, in situ microphysical probes, microwave radiometers, and sunphotometers.

4.3. Cloud Optical Property Retrieval Subsystem

4.3.1. Introduction

Cloud microphysics, phase and particle shape and size distribution determine the cloud optical depth and ice or liquid water path when integrated over the cloud thickness. These properties affect the emittance and bidirectional reflectance of the cloud. Cloud microphysics and macrophysics (areal extent, thickness, and altitude) determine the amount of radiation transmitted to the surface or to a lower atmospheric layer and the amount of absorption within the cloud layer. Therefore, the conversion of the

CERES radiances to flux, especially for the solar channel, depends on the cloud microphysics. Computation of the transmitted fluxes for the CERES estimation of atmospheric radiative divergence or surface heating also requires a quantification of the microphysical parameters.

From a climate perspective, it is important to know the global and climatological variability of cloud microphysical properties and to be able to relate them to radiative fluxes and cloud macrophysical properties. As an example, there is considerable interest in determining whether anthropogenic sources of cloud condensation nuclei significantly change the Earth radiation balance by altering the microphysical characteristics of clouds (e.g., Twomey 1977; Charlson et al. 1987; Wigley 1989). Such issues and how they may affect future climates can only be addressed through modeling studies. In climate models, such as GCM's, water vapor is condensed or frozen in a given time step. This mass of water releases latent heat and alters the radiative flux fields. The cloud particle size distribution, phase, and shapes determine how the cloud affects the flow of radiation. The particle size distribution, which can be expressed in terms of an effective radius or diameter, primarily affects the scattering and absorption efficiencies of the cloud particles (van de Hulst 1957) and defines the cross section normal to the incident flux. Particle shape primarily affects the scattering phase function which ultimately determines how radiation is reflected from the cloud. Water phase governs the basic absorption properties and affects the scattering phase function through its relation to particle shape and through the index of refraction. To produce realistic clouds and radiation fields, a GCM must condense or freeze water in the proper locations and then must distribute the mass into the correct particle sizes and shapes. Some current GCM's employ parameterizations of radiation dependence on cloud particle size (e.g., Slingo 1989). The CERES measurements, the most complete simultaneous global observations of cloud microphysics and radiative fluxes yet proposed, will serve as an essential ground truth set to ensure that climate models accurately perform this critical function.

The CERES Cloud Optical Property Retrieval Subsystem (COPRS) will employ state-of-the-art methods to analyze the relevant spectral radiances available from the VIRS, MODIS, and AVHRR instruments operating during the CERES era. The primary goal of COPRS is to determine the phase, effective particle size, optical depth, liquid or ice water path, radiating temperature, pressure, and thickness of the cloud within a given CERES pixel. Although there are a wide variety of methods available, there is no single technique for deriving the COPRS products that applies in all cases. This subsystem uses state-of-the-art procedures to arrive at the most accurate values for each product. Thus, it will combine several algorithms to cover as many cases as possible. The composite algorithm described herein is a fluid entity subject to change as new research and/or limiting factors warrant.

4.3.2. Background

There are numerous approaches to the satellite remote sensing of cloud phase, optical depth, and particle size. All of the methods are based on the assumption of radiative transfer in a plane-parallel cloud. These techniques exploit the spectral dependence of water and ice extinction, using wavelengths at which absorption by water vapor and other gases is minimal. The parameters used to characterize these variations include the wavelength λ , the spectral single-scattering albedo $\tilde{\omega}_o = Q_s/Q_e$, the asymmetry parameter g , the spectral optical depth τ_λ , and the particle radius r . The extinction efficiency is $Q_e = Q_s + Q_a$. The scattering efficiency Q_s depends on the imaginary refractive index m_i and the size parameter $x = 2\pi r/\lambda$. For spherical particles and a given λ , Q_s increases monotonically with x from zero to a maximum value near $x = 6$, then oscillates asymptotically to a smaller constant value. The oscillations are smoothed out when Q_s is integrated over a typical cloud droplet size distribution $n(r)$, in which r may vary from 2 to 100 μm . The absorption efficiency Q_a and $\tilde{\omega}_o$ follow a similar variation without the oscillations for $m_i < 0.25$ (Hansen and Travis 1974), values held by water for $\lambda < 12.5 \mu\text{m}$ (Hale and Querry 1973). The variation with x becomes more monotonic for larger values of m_i . The asymptotic values of Q_e and $\tilde{\omega}_o$ for large particles are 2.0 and 0.53, respectively. The single-scattering albedo is

essentially 1.0 and Q_s varies by less than 20% for typical cloud particle sizes at the nearly conservative-scattering wavelengths spanning the visible spectrum ($\lambda < 1.0 \mu\text{m}$). For near-infrared wavelengths ($\lambda \sim 3 \mu\text{m}$) ice and liquid water become moderately absorbing and x ranges from about 3 to 150. Thus, there are significant changes in both Q_e ($\sim 50\%$) and $\tilde{\omega}_o$ ($\sim 26\%$) with changing particle size. At longer wavelengths, absorption is stronger, though still variable with particle size and wavelength.

The asymmetry parameter, which summarizes the scattering phase function, ranges from -1 to 1 . Zero indicates isotropy, $g = -1$ corresponds to backscattering, and $g = 1$ denotes complete forward scattering. For any given particle shape, g generally increases with increasing particle size because of the narrowing diffraction peak. Smaller particles tend to scatter a greater portion of the incident radiation back into the source direction. The asymmetry parameter, which depends on both the real and imaginary refractive indices, varies nonmonotonically in a fashion similar to Q_s . There is a relative minimum in g for $10 < x < 20$ and a relative maximum for $4 < x < 10$. Hansen and Travis (1974) may be consulted for additional details of the radiative properties of water droplets.

The spectral optical depth for a given size distribution over some distance is

$$\tau_\lambda = \pi Q_e \int_{z_1}^{z_2} N r_e^2 dz \quad (4.3-1)$$

where the effective radius is

$$r_e = \frac{\int_{r_1}^{r_2} r \pi r^2 n(r) dr}{\int_{r_1}^{r_2} \pi r^2 n(r) dr} \quad (4.3-2a)$$

$n(r)$ is the number density of droplets with radius r , and N is the total particle number density. To distinguish between water and ice clouds, r_e will be used for water clouds and the equivalent diameter

$$D_e = \frac{\int_{L_1}^{L_2} D(L) \pi A_e(L) n(L) dL}{\int_{L_1}^{L_2} \pi A_e(L) n(L) dL} \quad (4.3-2b)$$

will be used for ice clouds. The variable $D(L)$ is the volume equivalent diameter of the hexagonal ice crystal of length L and width d . It is assumed that there is a monotonic relationship between L and d for the hexagonal ice columns defined by Takano and Liou (1989). This yields a unique relationship between the cross-sectional area A_e of these randomly oriented columns (Takano and Liou 1989) and L . The parameters, τ_λ , r_e or D_e , $\tilde{\omega}_o$, and g affect the radiation absorbed, reflected, transmitted, and emitted by a given cloud. The dependence of the radiation field on these variables can be simulated using radiative transfer calculations. Cloud effective particle size, optical depth, phase, and cloud temperature can be determined from satellite-measured multispectral radiances by matching the radiances to the computed radiative transfer results.

The basic techniques for determining cloud phase, optical depth, and effective particle size can be divided into two groups that overlap: reflection and emission techniques. The former applies during daytime and only employs solar wavelengths. Emission techniques generally are applicable during any time of day because they rely primarily on radiation emitted at infrared and near-infrared wavelengths.

4.3.2.1. Solar Reflectance Methods

The spectral bidirectional reflectance or, simply, reflectance is

$$\rho_{\lambda}(\tau_{\lambda}; \mu_o, \mu, \phi) = \frac{I_{\lambda}(\mu_o, \mu, \phi)}{\mu_o \pi E_o \lambda} \quad (4.3-3)$$

where $E_o \lambda$ is the spectral solar irradiance and μ_o , μ , and ϕ are the solar zenith and viewing zenith angle cosines and the relative azimuth angles, respectively. Optical depth can be determined directly from the reflectance data in the absence of particle size information, if a particle size is specified. Rossow et al. (1985) assumed that all clouds can be interpreted as having $r_e = 10 \mu\text{m}$, an approach later used in the ISCCP analyses (Rossow et al. 1988) and in pre-ISCCP analyses of NOAA-5 SR data (Rossow et al. 1990). In those analyses, a value of $\tau_{0.65}$ is determined by matching the 0.65- μm (visible) reflectance to a set of model-generated reflectance tables developed for different cloud heights, surface albedos, and optical depths. Later analyses using FIRE data (Baum et al. 1992; Minnis et al. 1993a) indicated that significant improvement is obtained in the accuracy of the derived optical depths by using the hexagonal ice crystal phase functions of Takano and Liou (1989) for cirrus clouds. Minnis et al. (1993b) developed a parameterization that incorporated surface albedo and cloud height so that reflectance tables were only needed to account for optical depth. The gained computer storage space could be used to accommodate models with variable particle size.

A more accurate estimate of τ_{λ} can be made if the particle size, shape, and phase are known. One of the earliest applications of a reflection method for this purpose was performed by Hansen and Pollack (1970) who attempted to explain the spectral variation in aircraft reflectivity measurements (Blau et al. 1966) in terms of phase and particle size using theoretical computations. Twomey and Seton (1980) showed theoretically that mean radius and optical depth could be determined for optically thick clouds using the scaled optical depth $\tau_{\lambda}' = (1 - \tilde{\omega}_o' g) \tau_{\lambda}$ and the scaled single-scatter albedo $\tilde{\omega}_o' = \tilde{\omega}_o (1 - g) / (1 - \tilde{\omega}_o g)$. A measurement of reflectance at a conservative-scattering wavelength could be used to determine τ_{λ}' , while r_e could be estimated using simultaneous measurements of reflectance at $\lambda = 1.6$ or $2.2 \mu\text{m}$. Later comparisons of aircraft reflectance measurements and calculations at $\lambda = 0.75, 1.0, 1.2,$ and $2.25 \mu\text{m}$ were relatively unsuccessful in matching the data with theory at all four wavelengths simultaneously (Twomey and Cocks 1982). Twomey and Cocks (1989) utilized an improved instrument and a multispectral minimum difference method to match theory and measurements much more closely for the same wavelengths plus $\lambda = 1.66 \mu\text{m}$.

Coakley et al. (1987) and Radke et al. (1989) showed that reflectance measurements at $3.7 \mu\text{m}$ could be used to detect ship tracks in marine stratus clouds because the droplet radii decreased in the portion of the cloud affected by the ship's exhaust. They also showed that an increase in the reflectance ratio, $\rho_{0.74} / \rho_{2.2}$, accompanied the decrease in radius measured with in situ probes. Using theoretical calculations at $0.75, 1.65, 2.16,$ and $3.70 \mu\text{m}$ and a minimum difference method employing the scaled optical depth $\tau' = (1 - g)\tau$ and the similarity parameter $s = [(1 - \tilde{\omega}_o) / (1 - \tilde{\omega}_o g)]^{1/2}$, Nakajima and King (1990) showed that measurements of reflectance at $0.75 \mu\text{m}$ and at either of the other wavelengths could be used to solve for r_e and τ_{λ} . However, a third channel was found to be desirable for removing ambiguities arising from the nonmonotonic variation of $\tilde{\omega}_o$ with r_e . They also found that the retrieved value of r_e corresponds to the effective radius for some upper portion of the cloud that depends on the cloud thickness. Thus, r_e requires some adjustment to estimate the effective radius for the entire cloud. Later analyses of aircraft observations at $0.75, 1.65,$ and $2.16 \mu\text{m}$ (Nakajima et al. 1991) over stratocumulus clouds produced excellent correlation between the remotely sensed, center-adjusted effective radii and the in situ particle sizes (Fig. 4.3-1). Although the remotely sensing analysis apparently overestimated r_e , the results clearly demonstrated the potential of this method. Further examination of the results indicated that the water vapor absorption at 1.65 and $2.16 \mu\text{m}$ needed additional study and that there are some significant disagreements between the aircraft probes used to measure particle sizes in the clouds. Wielicki et al. (1990) estimated particle sizes for water and ice clouds from Landsat observations at

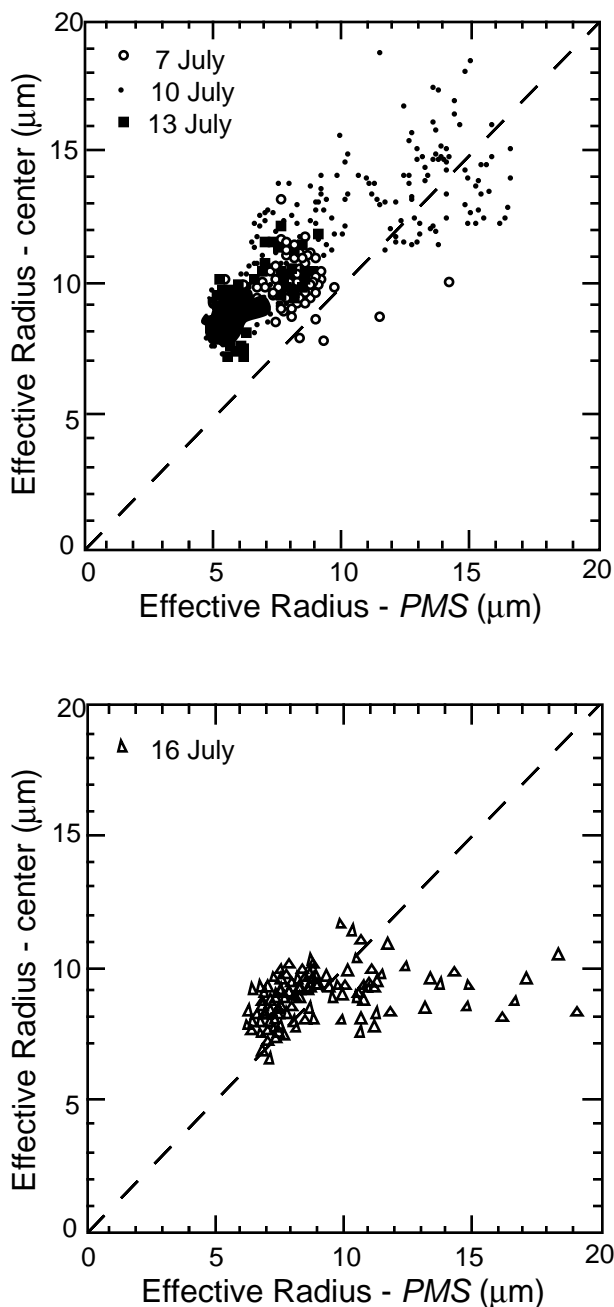


Figure 4.3-1. Effective radius derived from remote sensing and adjusted to center of cloud compared with values obtained from in situ measurements obtained using all three PMS probes. The top panel is based on ER-2 MCR measurements, while the bottom panel is from LANDSAT-5 TM data. All measurements were taken during 1987 off the coast of California during the FIRE Marine Stratocumulus Intensive Observing Period (adapted from Nakajima et al. 1991).

$\lambda = 0.83, 1.65, \text{ and } 2.21 \mu\text{m}$ by matching ratios of the reflectances to theoretical calculations. For water clouds, they found good agreement between the values of r_e derived from in situ data and the $0.83\text{-}\mu\text{m}/2.21\text{-}\mu\text{m}$ reflectance ratios. Rawlins and Foot (1990) used reflectances from aircraft measurements at $\lambda = 1.04, 1.24, 1.55, 2.01 \mu\text{m}$ to derive values of r_e that were 20% to 50% greater than their in situ counterparts. Differences between the in situ and remotely sensed data have not yet been entirely resolved as there are uncertainties in the instrumental results related to detection capabilities and in the remotely sensed data because of the effects of the vertical variation of r_e within the cloud.

Cloud phase can be determined by comparing the ratios of reflectances at two wavelengths: one that is a conservative scatterer for both ice and water and one that has strong absorption for ice and weak absorption for water. This type of approach was suggested by the theoretical calculations of Hansen and Pollack (1970) and other researchers. Curran and Wu (1982) used this approach to determine the presence of supercooled water clouds from Skylab measurements of reflectance at 1.61 μm . Masuda and Takashima (1990) demonstrated theoretically that a combination of measurements at 0.63 or 0.86 and 1.61 μm would be best for determining phase. Wielicki et al. (1990) found that the 2.21- μm /0.83- μm and the 1.65- μm /0.83- μm Landsat reflectance ratios could effectively distinguish between ice and water clouds when used together. King et al. (1992) showed that distinctly different 1.63- μm /0.75- μm reflectance ratios are measured over water and ice clouds. The water cloud reflectance ratio is about half that of the ice cloud. The ratio techniques are continually being improved and developed. They will be useful for the TRMM/VIRS and MODIS instruments but not for AVHRR.

4.3.2.2. Thermal Infrared Emittance Techniques

The simple model of brightness temperature usually employed in satellite remote sensing of clouds is that the observed radiance is

$$B_{\lambda}(T_{\lambda}) = [1 - \varepsilon_{\lambda}(\mu, \tau_{\lambda})][(1 - \varepsilon_{s\lambda})B_{\lambda}(T_{D_s}) + \varepsilon_{s\lambda}B_{\lambda}(T_s)] + \varepsilon_{\lambda}(\mu, \tau_{\lambda})B_{\lambda}(T_{cld}) \quad (4.3-4)$$

where T_{λ} is the equivalent blackbody temperature, T_s is the surface temperature, T_{cld} is the cloud temperature, T_{D_s} is the equivalent blackbody temperature of the downwelling radiance at the surface, B is the Planck function, $\varepsilon_{s\lambda}$ is the surface emittance, and the effective cloud emittance ε_{λ} approaches unity as the cloud becomes optically thick. If scattering is neglected,

$$\varepsilon_{\lambda} = 1 - \exp(-\tau_{a\lambda}/\mu) \quad (4.3-5)$$

where the absorption optical depth $\tau_{a\lambda} = (1 - \tilde{\omega}_o)\tau_{\lambda}$. The quantity $\varepsilon_{s\lambda}B_{\lambda}(T_s)$ can be replaced in many instances with $B_{\lambda}(T_{cs\lambda})$, where $T_{cs\lambda}$ is the clear-sky temperature. It includes the attenuation of the atmosphere which is not explicitly included in (4.3-4). For semitransparent clouds, it is possible to estimate ε_{λ} and T_{cld} from simultaneous measurements at two different wavelengths λ_1 and λ_2 , if $T_{cs\lambda}$ and the relationship between ε_{λ_1} and ε_{λ_2} is known and $\varepsilon_{\lambda_1} \neq \varepsilon_{\lambda_2}$. The surface emittance is generally assumed to be unity for longer wavelengths. It may be as low as 0.9 for some surfaces at the near-infrared wavelengths. If ε_{λ} is known, then τ_{λ} can be determined from either (4.3-5) or some other function that relates the two quantities. If T_{cld} is known—from some other source or a third wavelength—it is theoretically possible to determine r_e and τ_{λ} . As in the case for reflectance methods, the optical properties of clouds need to be different at each of the involved wavelengths. Hunt (1973) showed that the cloud emittance at 3.7 μm is more sensitive to changes in optical depth and particle size than at longer wavelengths such as 11 or 12 μm . Liou (1974) demonstrated that the optical properties of cirrus varied between 11 and 12 μm . These three spectral channels have been used on meteorological satellites and, therefore, have received much of the attention for deriving cloud properties. Some techniques make use of the brightness temperature difference BTD_{i-j} between T_i and T_j to provide some information about the particle size and optical depth. The subscripts i and j can refer to sensor channel numbers or their nominal wavelengths. The AVHRR channels 3, 4, and 5 have nominal wavelengths of 3.73, 10.8, and 12.0 μm .

Inoue (1985) developed a method using BTD_{4-5} and an implicit mean particle size to determine ε_4 and, therefore, τ_4 from AVHRR channels 4 and 5 taken over semitransparent cirrus clouds. Wu (1987) developed an algorithm to derive cirrus effective cloud fraction $\varepsilon_{11}C$ and T_{cld} using the HIRS2 3.7-, 4.0-, and 11- μm data. d'Entremont (1986) exploited the variation of AVHRR BTD_{3-4} with particle size to determine the presence of low clouds and fog at night. Ackerman and Stephens (1987) further explained the phenomena that permit the estimation of particle size from measurements of radiation simultaneously at two wavelengths: one strongly absorbing and one weakly absorbing. Prabhakara et al. (1988) used $BTD_{10.8-12.6}$ from the 10.8- and 12.6- μm IRIS data taken by the Nimbus-4 satellite as

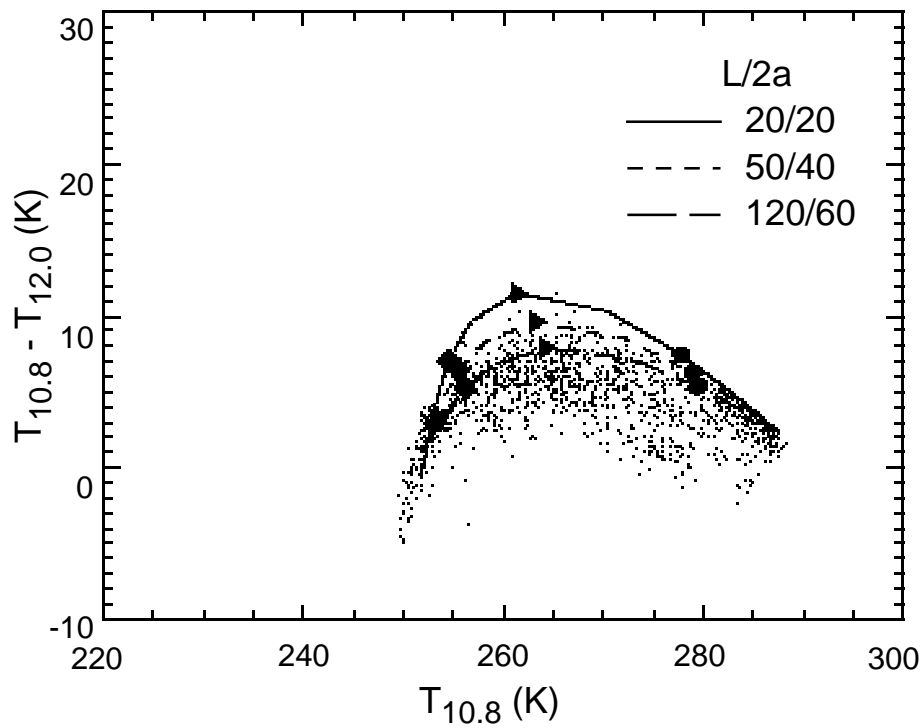
indices for the distribution of optically thin cirrus clouds. Ackerman et al. (1990) used ratios of the mass absorption coefficients derived from 10.1- and 12.0- μm HIS measurements to estimate cirrus cloud particle sizes in terms of ice-sphere effective radius. Liou et al. (1990a) used an iterative technique to estimate cloud temperature and optical depth from 6.5- and 11- μm radiances taken over high-altitude cirrus clouds. From theoretical calculations using spheres and cylinders to represent cirrus particles, Parol et al. (1991) concluded that the AVHRR BTD_{4-5} depends significantly on particle shape but not so much on phase. They found that scattering should be taken into account in the interpretation of the BTD 's. Takano et al. (1992) developed a parameterization to compute the optical properties of cirrus clouds at any infrared wavelength using a combination of hexagonal ice crystals and spheroids to represent the cirrus cloud particles. The latter are used for large size parameters x , while the former are invoked for small x . The Takano et al. (1992) model matched observations of BTD_{11-12} much more closely than the spherical representations. Lin and Coakley (1993) advanced a method to derive a particle size index for single-layer cloud decks using radiative transfer model fits to clusters of collocated AVHRR channel 4 and 5 pixels. Their method simultaneously solved for the emittance and cloud fraction by computing an envelope of solutions based on a single effective radius and cloud temperature for the pixel cluster. Ou et al. (1993) developed a method to derive $\tau_{0.67}$, T_{cld} , and D_e from nighttime AVHRR measurements of $T_{3.7}$ and $T_{10.9}$. They assumed that particle size depended on cloud temperature according to the parameterization of Heymsfield and Platt (1984) and developed a parameterization of $B_{11}(T)$ in terms of $B_{3.7}(T)$. Baum et al. (1994) successfully modeled $BTD_{3.7-11}$ and BTD_{11-12} values from AVHRR observations taken over oceanic cirrus, stratocumulus, and a cirrus-stratocumulus mix. Their models are based on the results of Takano et al. (1992), Liou et al. (1990b), Minnis et al. (1993b), and Mie scattering calculations. They found that a combination of all three channels may be used to determine T_{cld} , τ_λ , and r_e or D_e simultaneously.

Infrared spectra may be used to determine cloud phase, though not as easily as solar spectra. Ackerman et al. (1990) demonstrated that BTD_{11-12} and BTD_{8-11} may be used to determine the cloud phase for optically thin clouds, at least. The analyses of Baum et al. (1994) showed that a combination of $BTD_{3.7-11}$ and BTD_{11-12} has the potential for separating ice and water clouds for many particle sizes for $\tau_{0.65} < 6$. Figures 4.3-2 and 4.3-3 adapted from Baum et al. (1994) show the BTD 's from AVHRR observations for a cloud deck with $T_{cld} = 250$ K. The theoretical values of $BTD_{3.7-11}$ for ice clouds, shown as the curves in Figure 4.3-2(a), are generally greater than those for water clouds (Fig. 4.3-3(a)) while the opposite is true for BTD_{11-12} (Figs. 4.3-2(b) and 4.3-3(b)). This potential for phase determination is currently under study.

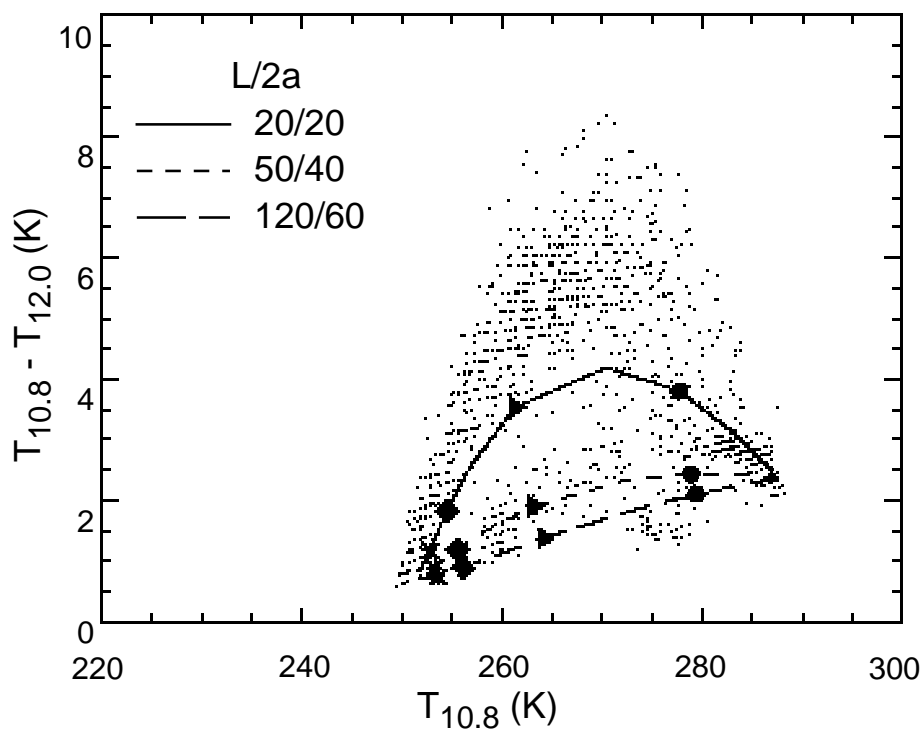
4.3.2.3. Combined Thermal Emittance-Solar Reflectance Methods

There are mixed methods that use both thermal and solar channels and, sometimes, an overlapped solar-thermal channel. The simplest of the mixed techniques, a bispectral visible-infrared analysis, is the form most widely used. In this approach, optical depth is derived from the visible reflectances using an implicit or explicit model of the cloud radiative properties. The infrared (11 μm) emittance, derived from the visible optical depth, is used to correct the observed T_{11} using (4.3-4) to obtain T_{cld} . Reynolds and Vonder Haar (1977) used an empirical model that represents an implicit cloud model to relate cloud albedo to ε_{11} . Rossow and Lacis (1990) used a theoretical-empirical approach and a single cloud microphysical model, a method also used by the ISCCP (Rossow et al. 1988). Minnis et al. (1993b) employed a purely theoretical method using various cloud microphysical models. Those bispectral methods are relatively effective and applicable to most operational satellite datasets. They do not, however, yield any information about particle size or phase other than what is assumed. To obtain particle size, a third channel or some other type of information is needed.

Arking and Childs (1985) pioneered the use of visible, infrared, and the 3.7- μm data to retrieve cloud fraction C , $\tau_{0.65}$, r_e , and T_{cld} for each pixel. Their method uses a pixel clustering technique to determine T_{cld} for a scene. All pixels outside the cluster are assumed to have a cloud temperature equal

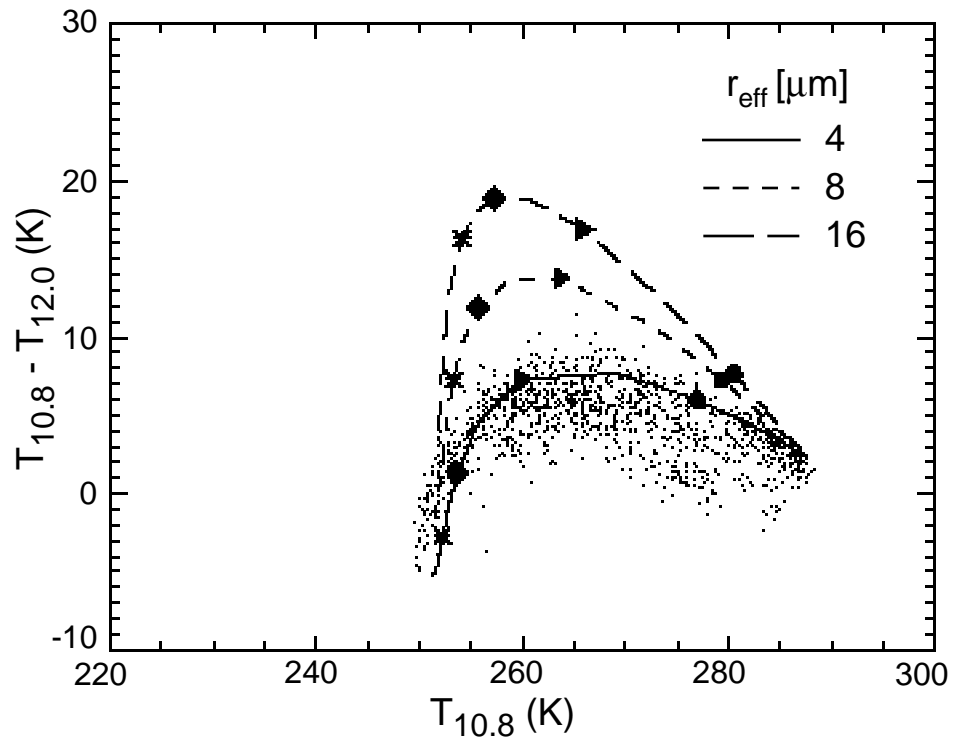


(a) $BTD_{3.7-11}$.

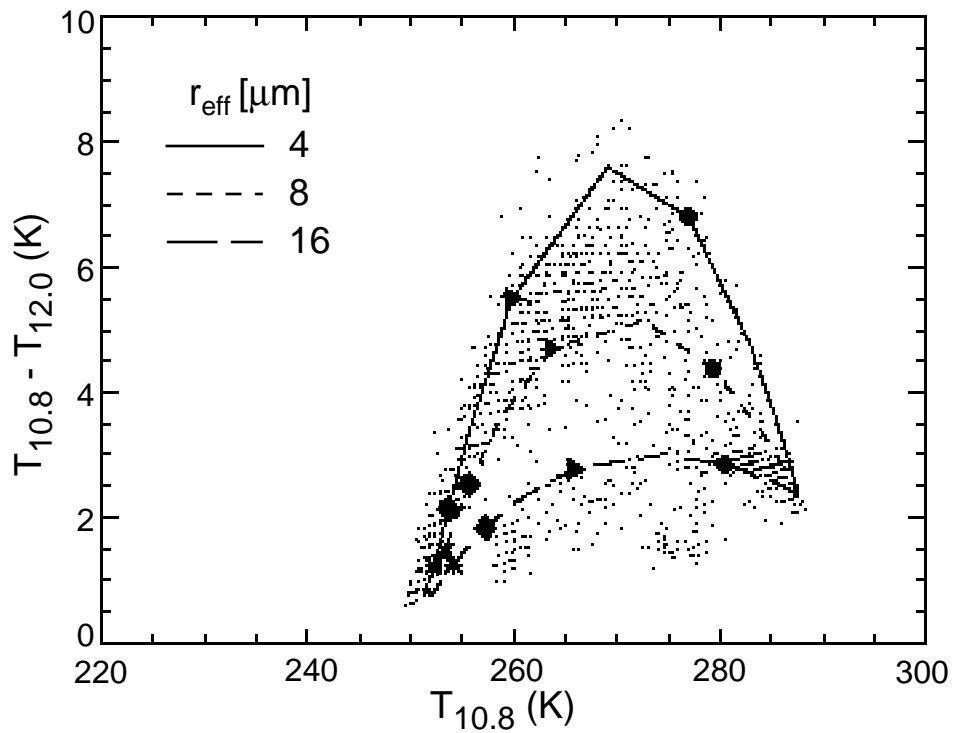


(b) BTD_{11-12} .

Figure 4.3-2. Comparison of theoretical results assuming cloud composed entirely of hexagonal ice crystals with AVHRR data taken over the northwest Atlantic at 0606 UTC, April 16, 1989. The ice crystal length-to-width ratios $L/2a$ are given in $\mu\text{m}/\mu\text{m}$. The circles, triangles, diamonds, and asterisks refer to the $10.8\text{-}\mu\text{m}$ optical depths of 0.5, 2, 4, and 6, respectively (adapted from Baum et al. 1994).



(a) $BTD_{3.7-11}$.



(b) BTD_{11-12} .

Figure 4.3-3. Same as Figure 4.3.2, except assuming cloud composed entirely of supercooled water droplets in the model calculations (adapted from Baum et al. 1994).

to the scene value of T_{cld} . The difference between the observed T and T_{cld} for each pixel outside the cluster is interpreted as a cloud fraction $C < 1$, so C is computed for each pixel. The optical depth and spherical particle size category are determined for each pixel using the visible and 3.7- μm radiances with T_{cld} and C . The use of the 3.7- μm data during the day complicates (4.3-4) because there is some solar reflectance at that wavelength. The observed radiance has an additional term

$$B(T) = \varepsilon(\tau, r_e; \mu)B(T_{cld}) + [1 - \varepsilon(\tau, r_e; \mu)]\varepsilon_s B(T_{cs}) \\ + \frac{\mu_o E_o}{\pi} \left\{ \rho(\tau, r_e; \mu_o, \mu, \phi) + \frac{[1 - \alpha_c(\tau, r_e; \mu_o)][1 - \alpha_c(\tau, r_e; \mu)]\rho_s(\mu_o, \mu, \phi)}{1 - \alpha_{sd}\alpha_{cd}(\tau, r_e)} \right\} \quad (4.3-6)$$

where the subscript λ has been dropped for simplicity. The effective emittance includes both the absorption and scattering effects of the cloud. The surface bidirectional reflectance and diffuse albedo are ρ_s and α_{sd} , respectively. The cloud directional and diffuse albedos are α_c and α_{cd} , respectively. These terms are formally defined by Minnis et al. (1993b). Atmospheric absorption and scattering effects are neglected in equation (4.3-6), which can be used for any wavelength since E_o and ε approach zero for infrared and visible wavelengths, respectively.

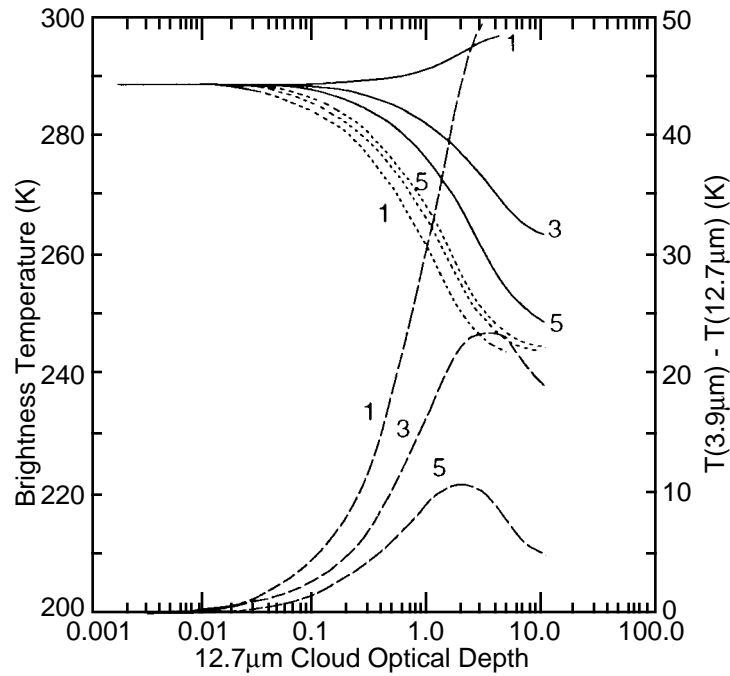
Stone et al. (1990) continued the development of the technique using *BTD*'s between infrared window (10–12.7 μm) and near-infrared (3.5–4.0 μm) radiances by comparing model calculations of daytime *BTD*'s for various sizes of ice spheres to GOES and AVHRR data. Figure 4.3-4 shows the Stone et al. (1990) model calculations of $T_{3.9}$, $T_{12.7}$, and $BTD_{3.9-12.7}$ for three different effective ice sphere sizes (as defined by Stone et al. 1990, model 1: $D_e = 8 \mu\text{m}$; model 3: $D_e = 32 \mu\text{m}$; model 5: $D_e = 128 \mu\text{m}$). The daytime $BTD_{3.9-12.7}$ values (Fig. 4.3-4(a)) are more sensitive to changes in D_e than their nocturnal counterparts (Fig. 4.3-4(b)) because of the reflected component in the 3.9- μm radiances. This increased sensitivity is also found for liquid water clouds. Han (1992) exploited the daytime sensitivity of T_3 to particle size to construct the first semiglobal survey of r_e for water clouds using ISCCP AVHRR data. His method explicitly solves (4.3-6) through an iterative technique for $\tau_{0.67}$, T_{cld} , and r_e using $\rho_{0.67}$, $T_{3.73}$, and $T_{10.8}$ and a set of lookup tables derived from radiative transfer calculations. The lookup tables are limited to $\mu > 0.9$, $\mu_o > 0.2$, and liquid water droplets. The method is applied only to pixels having $T_{cld} > 273 \text{ K}$. This technique has produced reasonable results over the middle and low latitudes where it was applied to a set of AVHRR data.

Young et al. (1993) and Young et al. (1994) expanded on the approach of Han (1992) by using models of reflectance and emittance developed by Minnis et al. (1994) for all angles, cloud and surface temperatures, cloud phase, optical depths, and particle sizes. Their iterative scheme is similar to that of Han (1992) but it contains some additional features. The Young et al. (1994) method selects an ice or water model automatically using the initial comparison of the computed $T_{3.73}$ with the observed value. Mie scattering calculations are used for the water droplets. The ice cloud models are based on the hexagonal crystal and spheroid parameterizations of Takano and Liou (1989), Minnis et al. (1993b), and Takano et al. (1992). The initial applications of this methodology compare well with in situ and ground-based radar measurements of particle size taken during FIRE II and ASTEX.

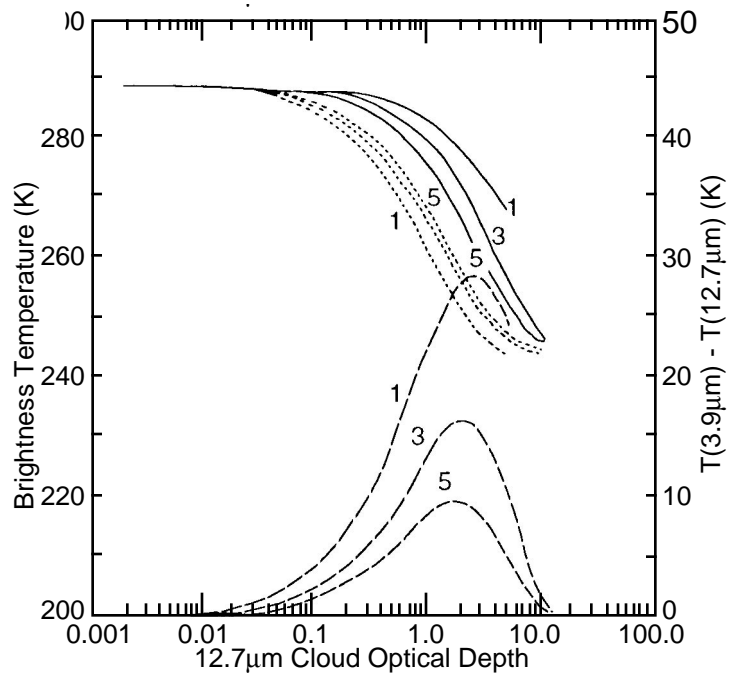
Another mixed technique, applicable only to water clouds over ocean in daylight, involves the simultaneous use of microwave radiances to infer liquid water path W_{liq} and visible radiances to derive optical depth. Minnis et al. (1992) used radiative transfer models of visible reflectance in terms of $\tau_{0.65}$ and r_e and

$$r_e = \frac{3Q_e W_{liq}}{4\delta_{liq}\tau_{0.65}(\rho, r_e)} \quad (4.3-7)$$

to obtain r_e from surface-based microwave measurements of W_{liq} and GOES visible data. The density of liquid water is δ_{liq} . This equation is a generalized version of an approximation by Stephens (1978) in



(a) Daytime.



(b) Nighttime.

Figure 4.3-4. Composite plots of 3.9-μm and 12.7-μm brightness temperature and their differences as functions of the 12.7-μm optical depths for model cirrus clouds during (a) daytime and (b) nighttime situations. The numbers next to each curve relate to model values of effective particle size. Models 1, 3, and 5 refer to effective ice-sphere radii of 4, 16, and 64 μm, respectively. The solid and short-dashed curves are for the 3.9-μm and 12.7-μm temperatures, respectively. The long-dashed curves relate to the temperature differences (adapted from Stone et al. 1990).

which Q_e is assumed to have a value of 2 for visible wavelengths. The extinction efficiency actually varies from 2.3 to 2 for r_e ranging from 2 to 32 μm . Minnis et al. (1992) found excellent agreement between their derived effective radii assuming $Q_e = 2$ and the available in situ data taken off the coast of California during the July 1987 FIRE stratocumulus experiment. Young et al. (1992) applied this visible-microwave approach to derive r_e from nearly coincident DMSP SSM/I microwave data and GOES visible radiances. The resulting mean value of r_e was 9.2 μm , identical to that derived using the technique of Young et al. (1994) applied to nearly coincident AVHRR data. The values from the visible-microwave method, however, ranged from 6 to 14 μm compared to 7 to 11 μm from the AVHRR data. The most likely cause of the range differences may be the sensitivity of the reflectance techniques to the droplets in the top of the cloud (cf. Nakajima and King 1990). Further, the visible-microwave method must simultaneously account for the reflectance and liquid water path of the entire cloud. In nonprecipitating conditions, stratiform clouds tend to have smaller droplets at the bottom. The opposite situation is likely to occur for precipitating clouds. Additional research is required to reconcile the discrepancies between the two methods.

4.3.3. Data and Model Database

The primary input data to COPRS include the following elements from a CERES cloud-algorithm unit data block (16×16 imager pixels): mean $T_{cs\lambda}(L)$, $\rho_{cs\lambda}(L)$, $\alpha_{sd\lambda}(L)$, $T_{cs\lambda}(S)$, $\alpha_{sd\lambda}(S)$, and $\rho_{cs\lambda}(S)$, $T(p)$, $\tau_{\text{H}_2\text{O}\lambda}(p)$, τ_{aer} , τ_{O_3} , $E_{o\lambda}$ and μ_o , μ , and ϕ for the center of the block. The parenthetical L and S refer to land and sea, respectively. The clear-sky albedo is $\alpha_s(\mu_o)$ and the clear-sky diffuse albedo is α_{sd} . The spectral water vapor optical depth is $\tau_{\text{H}_2\text{O}\lambda}(p)$, and the visible aerosol and ozone optical depths are τ_{aer} and τ_{O_3} , respectively. The spectral radiances and geoclassification for each pixel in the data block are also included. These input elements have been described in detail in section 4.1. Other inputs derived in the section 4.2. subsystem are the clear, single-layer, or multiple-layer indices for each pixel and the values for the cloud layer temperatures for all layers detected for the eight surrounding data blocks.

To maintain a standard reference, optical depth is reported in terms of the visible channel optical depth, $\tau_{0.65}$. The optical depth at a given wavelength λ_1 for any effective particle size can be related to the optical depth at any other wavelength λ_2 by

$$\tau_{\lambda_1} = \tau_{\lambda_2} \frac{Q_{e\lambda_1}}{Q_{e\lambda_2}} \quad (4.3-8)$$

For simplicity, the wavelength subscript is dropped for the visible optical depth. It will continue to be used for other wavelengths. The AVHRR channel numbers 3, 4, and 5 will hereafter replace the wavelength designations for $\lambda = 3.7$, 10.9, and 11.9 μm , respectively.

The cloud solar radiance model database consists of lookup tables giving the spectral cloud reflectance $\rho_\lambda(r_e$ or $D_e; \tau; \mu_o, \mu, \phi)$, cloud albedo $\alpha_c(r_e$ or $D_e; \tau; \mu_o)$, and diffuse cloud albedo $\alpha_{cd}(r_e$ or $D_e; \tau)$ for the relevant channels: 0.63, 1.60, and 3.75 μm for VIRS and AVHRR (Minnis et al. 1993b; Minnis et al. 1994) plus 2.12 μm for MODIS. The lookup tables were constructed for $r_e = 2, 4, 6, 8, 12, 16,$ and 32 μm and $D_e = 23, 37, 64, 108,$ and 180 μm with $\tau = 0.25, 0.5, 1, 2, 3, 4, 8, 16, 32, 64, 96,$ and 128; $\mu_o = 1, 0.95, 0.85, \dots, 0.05$; $\mu = 1, 0.9, 0.8, \dots, 0.1$; and $\phi = 0, 7.5, 15, 30, 45, \dots, 165, 172.5, 180^\circ$. The optical depth range for 3.75 μm ends at $\tau = 32$ because the reflectance is essentially constant for greater optical depths. For bright backgrounds, a set of lookup tables giving the 0.65- μm reflectance at the top of the atmosphere has been developed for the same sets of angles. These lookup tables were computed for all of the water and ice clouds using surface albedos ranging from 0.20 to 0.80 in increments of 0.15 for $\tau = 0.25, 0.5, 1, 2, 3, 4,$ and 8 and $p = 1000, 700, 400,$ and 100. No water vapor or ozone absorption was included in these calculations.

Figure 4.3-5 shows examples of the cloud reflectance lookup tables normalized to the cloud albedo [i.e., the ratio $\rho_\lambda(\mu_o, \mu, \phi)/\alpha_c(\mu_o)$] for $r_e = 16 \mu\text{m}$ (Fig. 4.3-5(a)) and $D_e = 37 \mu\text{m}$ (Fig. 4.3-5(b)) for channel 3 with $\tau = 4$ and $\mu_o = 0.55$. The effective volume of these two particle distributions are close, but the diffuse albedos are 0.13 and 0.06, respectively. Although the reflectance patterns (Fig. 4.3-5) are somewhat similar, they show some distinct features typical of the differences between scattering from spheres and hexagonal crystals. The relative reflectance patterns for the visible channel (Fig. 4.3-6) are different than those in Figure 4.3-5, but the discrepancies between the ice and water reflectances are quite noticeable. In contrast to the $3.75\text{-}\mu\text{m}$ results, the visible-channel liquid-cloud diffuse albedo of 0.31 is less than the value of 0.42 for ice-cloud model. Cloud albedo α_c increases with decreasing particle size for both channel 3 and the visible channel as demonstrated in the reflectance plots of the models for $r_e = 4, 8, \text{ and } 16 \mu\text{m}$ in Figures 4.3-7 and for $D_e = 23, 41, \text{ and } 124 \mu\text{m}$ in Figures 4.3-8.

The cloud emittance models comprise a set of 75 coefficients for channels 3, 4, or 5 for the VIRS and AVHRR (Minnis et al. 1994) plus the $8.55\text{-}\mu\text{m}$ channel of MODIS. The following regression formula was fitted to effective emittances computed using (4.3-4) and radiances calculated with the adding-doubling radiative transfer model of Minnis et al. (1993b).

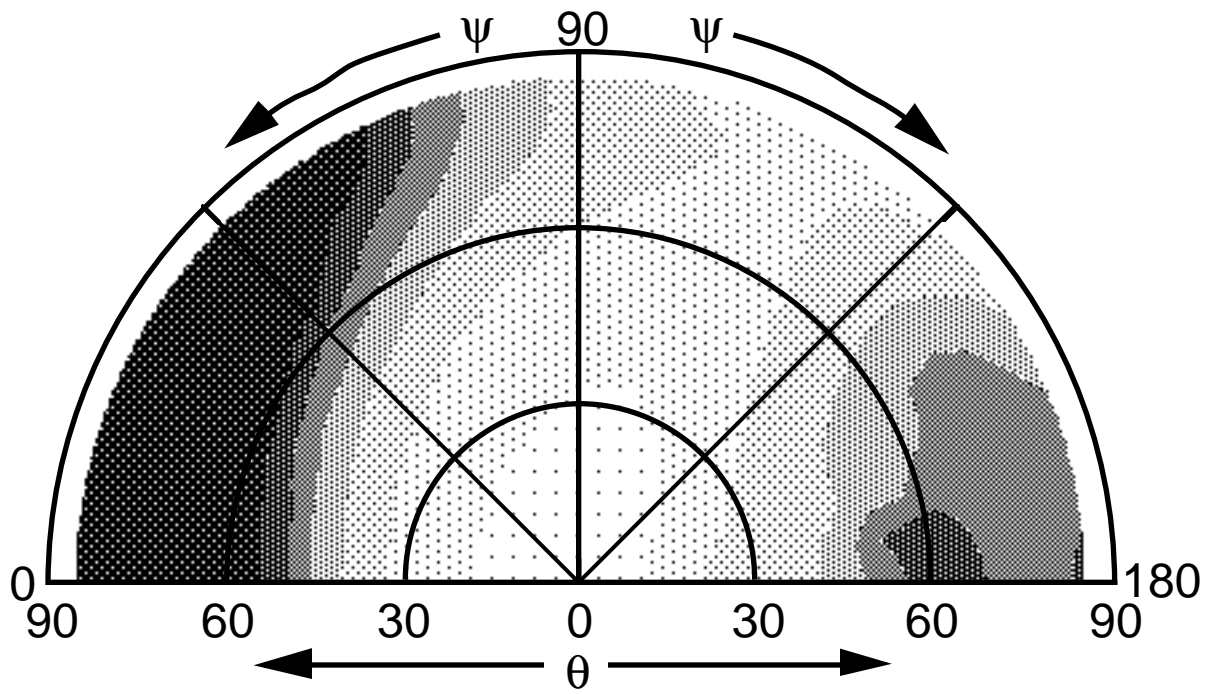
$$\varepsilon(\lambda, r_e) = a_0 + a_1 \{1/\ln(\Delta T)\} + a_2 \{1/\ln(\Delta T)^2\} \quad (4.3-9)$$

where $\Delta T = T_{cs} - T_{cld}$, $a_i = \sum b_j \tau^j$, and $b_j = \sum c_k \mu^k$, ($j = 0, 4$ and $k = 0, 4$). The visible optical depth is used in all cases. The standard error of this parameterization is $\leq 3\%$ for most of the particle distributions. Figure 4.3-9 shows the BTD_{3-4} and BTD_{4-5} computed using the effective emittances from (4.3-9) for hypothetical nocturnal clouds viewed from $\theta = 45^\circ$ at a temperature $T_{cld} = 255 \text{ K}$ over a clear scene having a brightness temperature of $T_{cs} = 300 \text{ K}$. Four clouds are represented, two comprising water droplets with effective radii $r_e = 6$ and $16 \mu\text{m}$ and the other two consisting of randomly oriented hexagonal ice crystals having effective diameters $D_e = 37$ and $180 \mu\text{m}$. As τ increases, the $10.8\text{-}\mu\text{m}$ temperature approaches T_{cld} . It is clear that, for both the water droplet and ice crystal models, $BTD_{3-4} > BTD_{4-5}$. This greater difference is typical for most cold clouds, and the ice models are obviously distinguishable from the water droplet models. Differences between BTD_{3-4} for $D_e = 37$ and $180 \mu\text{m}$ are smaller than those between BTD_{4-5} at the smaller optical depths (warmer brightness temperatures), while the reverse is true for larger optical depths. During the daytime, the BTD_{3-4} for $D_e = 37$ and $180 \mu\text{m}$ are always greater than BTD_{4-5} because of the solar contribution to the channel-3 radiance.

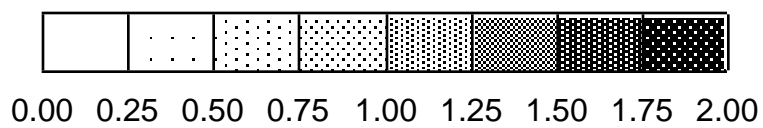
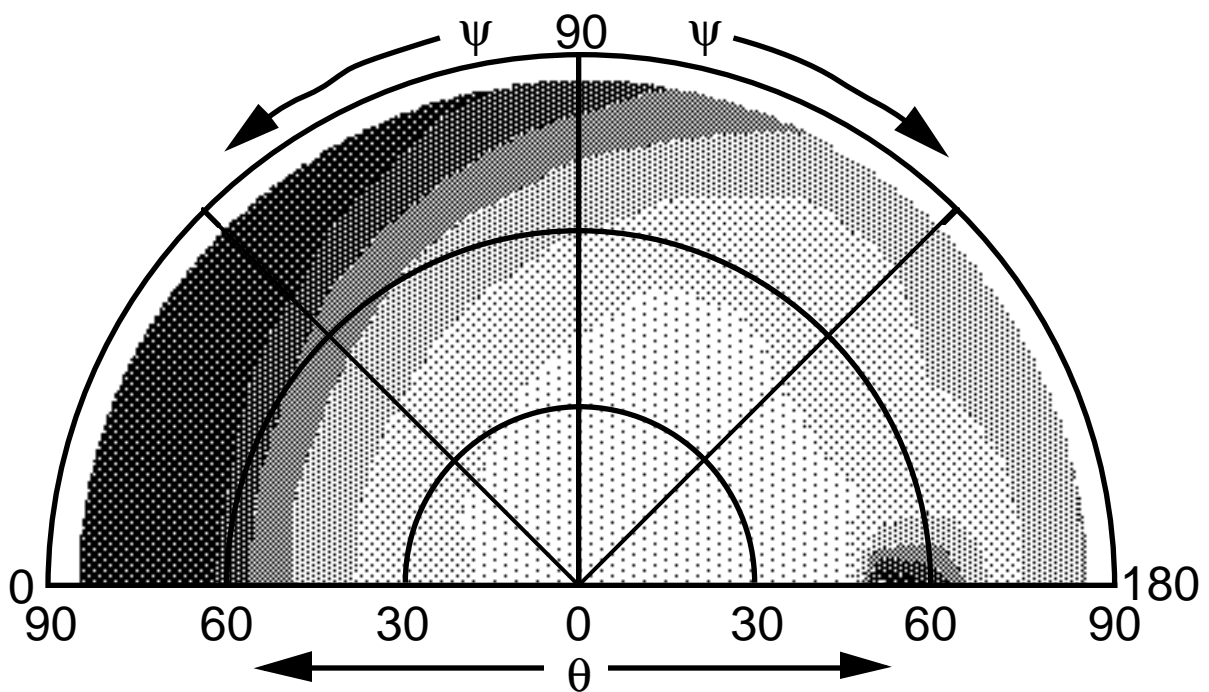
Atmospheric corrections for the solar channel are performed using the models and methods of Minnis et al. (1993b). Corrections for atmospheric water vapor are applied to the infrared and near-infrared channels using correlated-k fits (Kratz 1995; see also Appendix). When the models are applied, reflectances are computed for each appropriate channel at μ_o , μ , and ϕ for the center latitude and longitude of the data block over a range of particle sizes and optical depths for both land and ocean. Emittances are computed for the same particle sizes and optical depths at μ using the initial guess of T_{cld} . The model results are then corrected for atmospheric attenuation. A clear-sky bidirectional reflectance model and spectral surface emittance are required in the analyses.

4.3.4. Methodologies

The multispectral reflectance techniques are sensitive to a wide range of particle sizes but are limited to daytime. Emittance methods are applicable at all times, but they are sensitive to a smaller range of r_e and can be used only when the cloud is semitransparent. The 3-channel mixed methods are the only techniques available using current global satellite data and are applicable to a wide range of optical depths. They cannot be used at night, however, and are sensitive to a smaller range of particle sizes than the solar methods. There are also many other situations in which one or all of the techniques will fail to retrieve the desired parameters (see section 4.3.5.2.). To overcome these deficiencies, the COPRS will utilize all three approaches to arrive at the most reliable estimates of the cloud properties in as many situations as possible. For application to CERES/VIRS, the 3-channel reflectance-emittance techniques

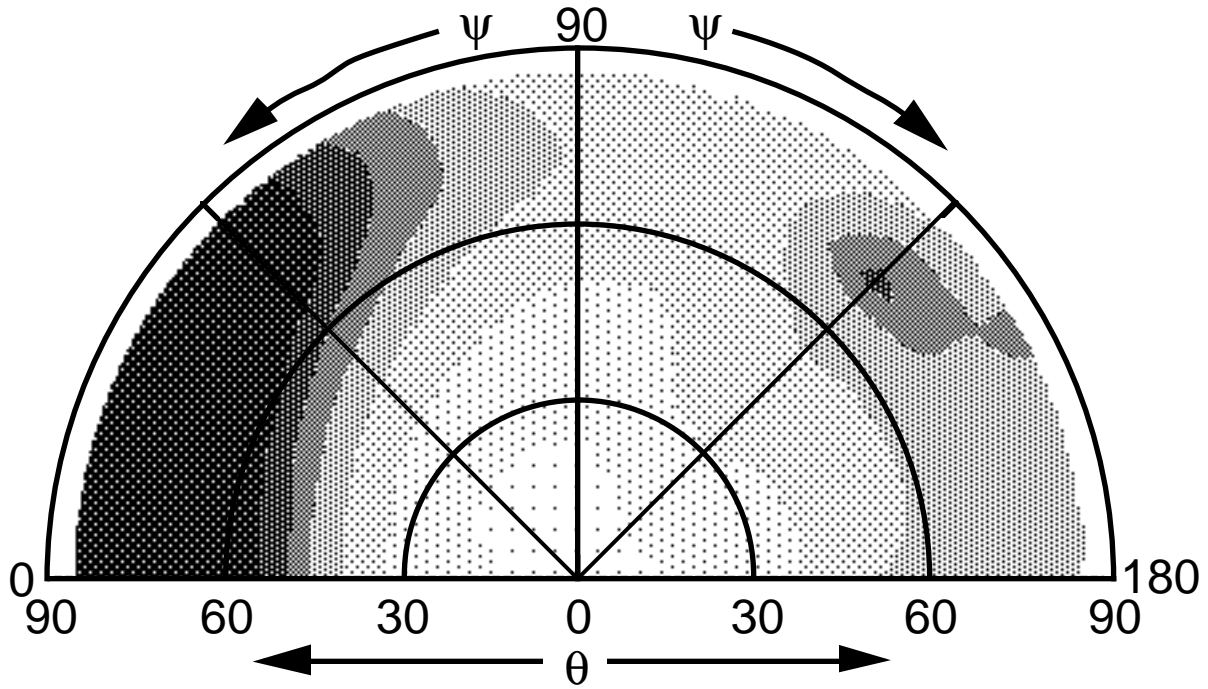


(a) $r_e = 16 \mu\text{m}$.

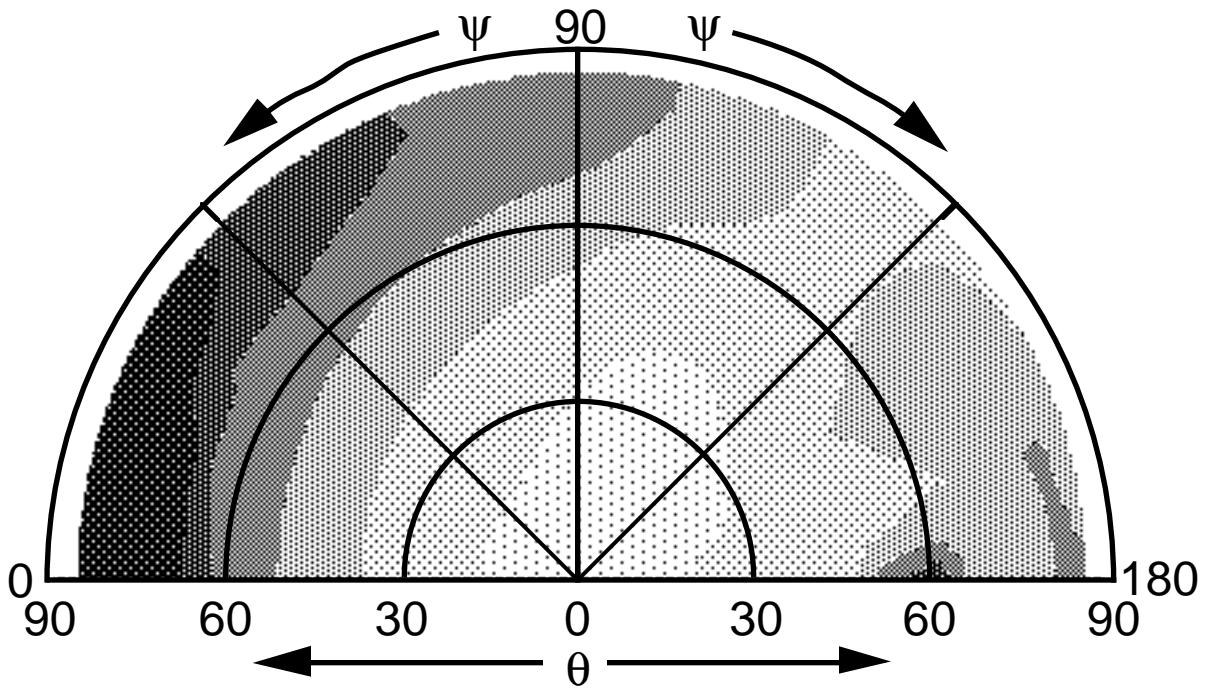


(b) $D_e = 37 \mu\text{m}$.

Figure 4.3-5. Normalized theoretical anisotropic reflectance values for $\tau = 4$, $\mu_o = 0.55$, and $\lambda = 3.75 \mu\text{m}$.

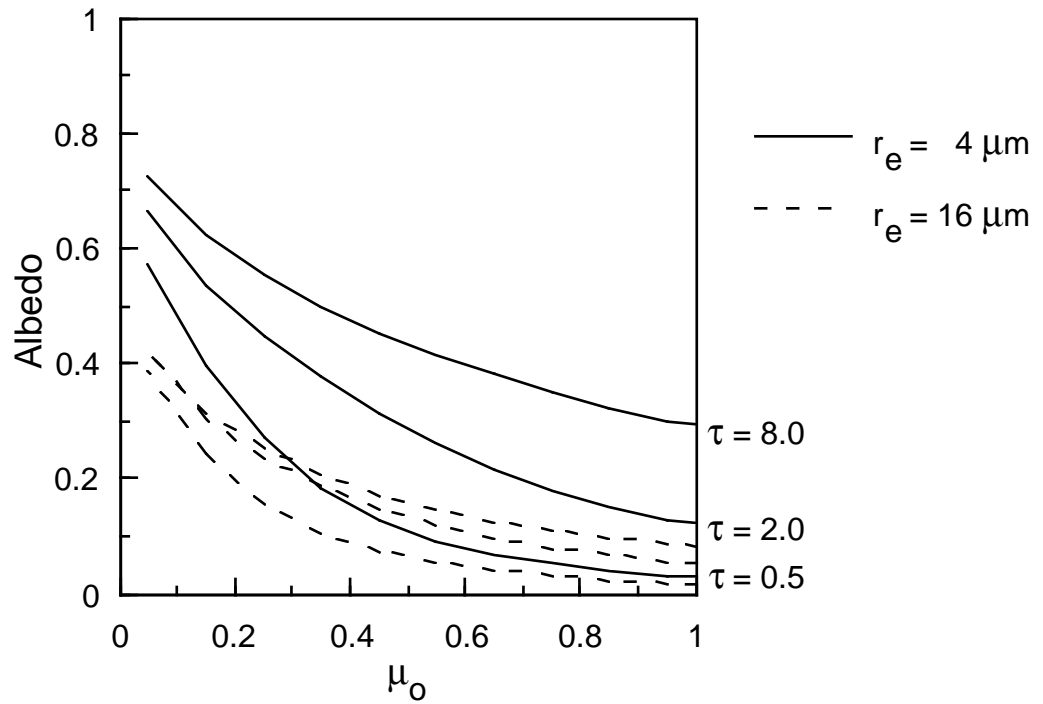


(a) $r_e = 16 \mu\text{m}$.

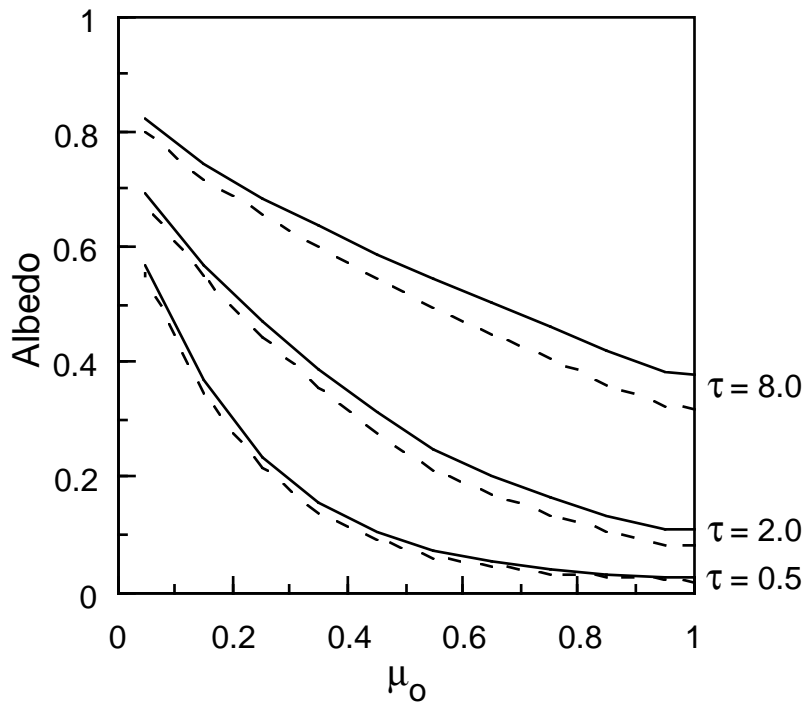


(b) $D_e = 37 \mu\text{m}$.

Figure 4.3-6. Normalized theoretical anisotropic reflectance values for $\tau = 4$, $\mu_o = 0.55$, and $\lambda = 0.65 \mu\text{m}$.

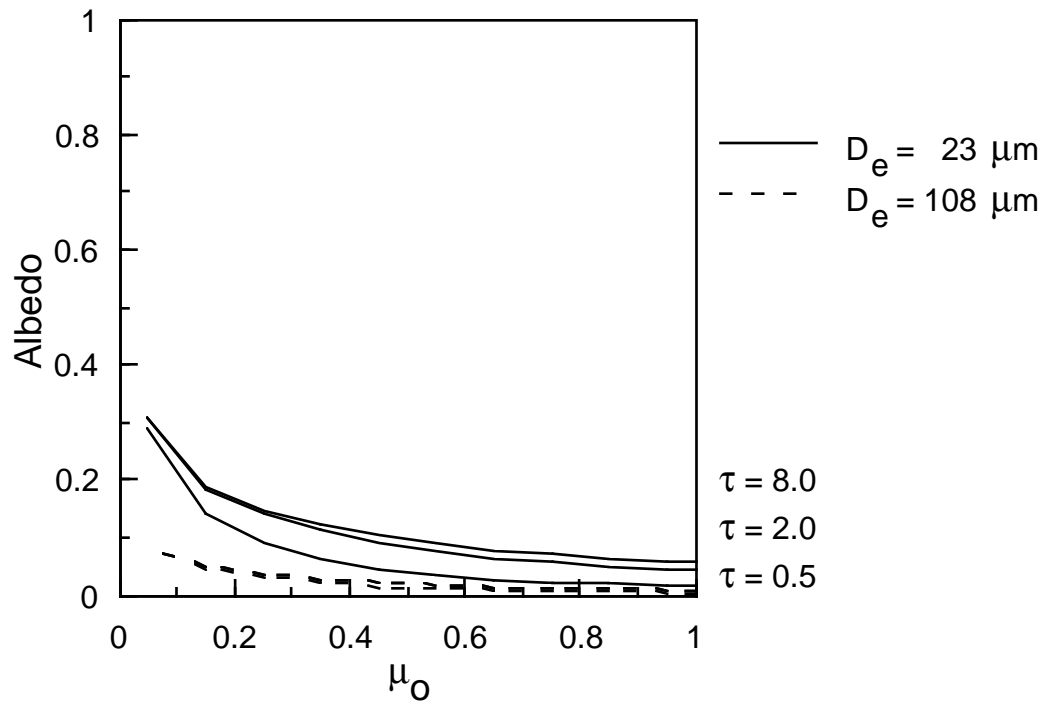


(a) $\lambda = 3.75 \mu\text{m}$.

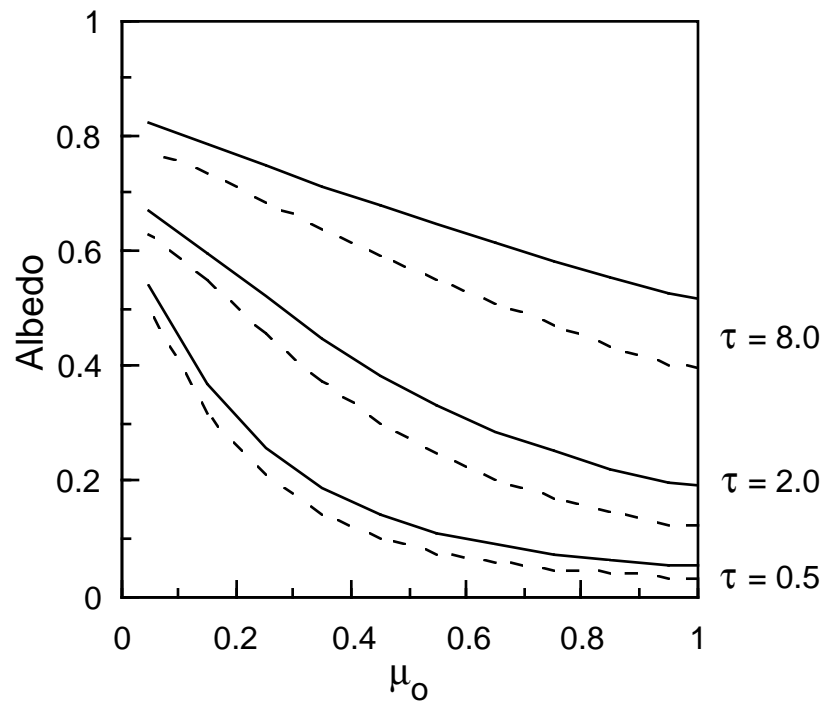


(b) $\lambda = 0.65 \mu\text{m}$.

Figure 4.3-7. Theoretical albedos for 4- μm and 16- μm water droplets.



(a) $\lambda = 3.75 \mu\text{m}$.



(b) $\lambda = 0.65 \mu\text{m}$.

Figure 4.3-8. Theoretical albedos for 23- μm and 108- μm ice particles.

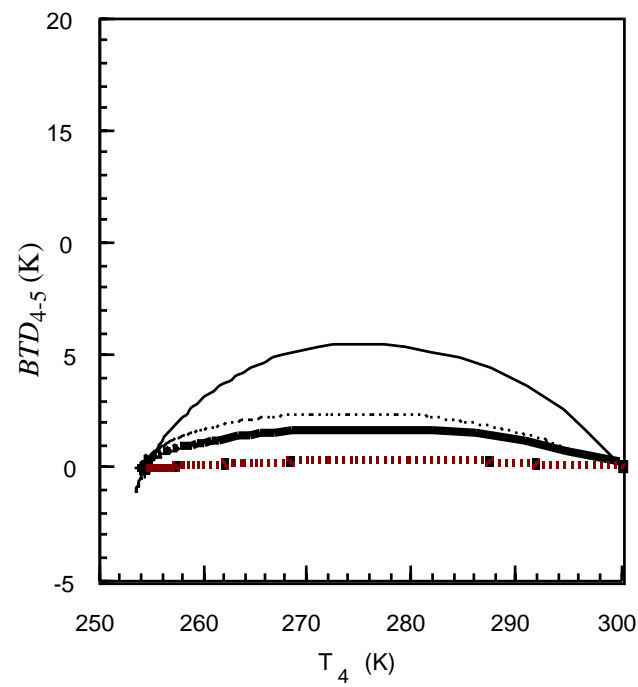
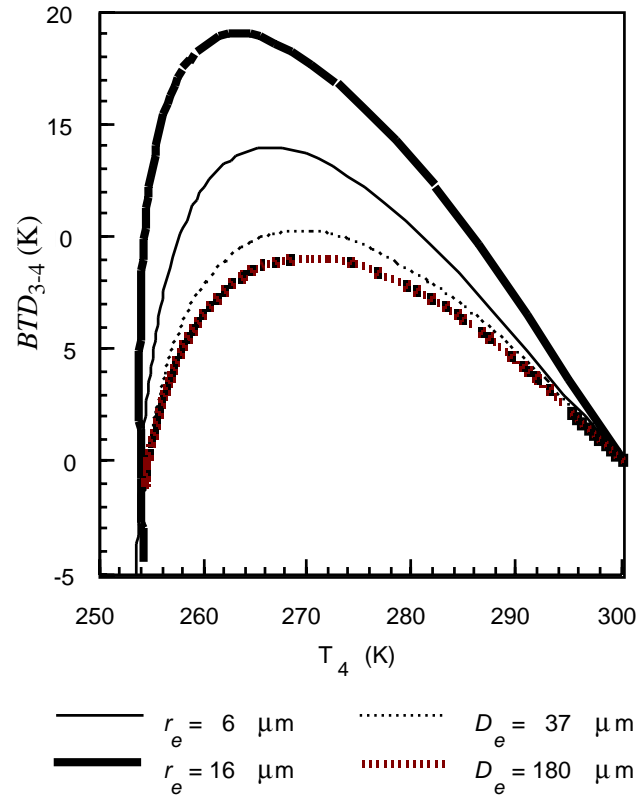


Figure 4.3-9. Theoretical brightness temperature differences for $T_{cld} = 255$ K, $\Theta = 45^\circ$.

will serve as the primary methods for simultaneous retrieval of optical depth, effective particle size, and phase. The reflectance methods generally rely on a 2.13- μm channel to determine particle size. This channel will be unavailable on VIRS. There is some skill in the reflectance methods, however, to determine particle size and phase using only the visible and 1.61- μm channels. Therefore, the reflectance method will be applied during the daytime to verify phase and whenever a solution is unavailable from the 3-channel method. When the MODIS is operating, it will be possible to apply a full-scale reflectance technique because of the wide choice of channels. Whenever the primary and secondary methods fail, a 3-channel infrared method is applied during the daytime. The same 3-channel infrared method is applied at night in most cases. For the Release-1 algorithm using VIRS, the three channels are 3.75, 10.8, and 12 μm . For MODIS, a 4-channel method will be possible because of the additional 8.55- μm sensor. In all cases, both day and night, the results derived from each method will be compared for consistency and to arrive at a single result. The decision-tree selecting the final values will incorporate information regarding the reliability of each technique for the given conditions.

4.3.4.1. Daytime Cloud Optical Depth, Particle Size, and Cloud Temperature

4.3.4.1.1. 0.65-3.75-10.9- μm method. Given ρ_{cs} (0.65), ρ_{cs} (3.75), T_{cs4} , and T_{cs3} , the phase, particle size, optical depth, and cloud temperature are evaluated for each pixel by iteratively solving first for τ using the observed visible reflectance $\rho_{0.65}$, second for T_{cld} using T_4 in (4.3-4), and finally using T_3 in (4.3-6) to obtain r_e . The optical depth is obtained by matching the observed reflectance to a parameterization of radiative transfer calculations of reflectance in terms of cloud optical depth. This model is

$$\rho_{0.65} = (\sum \rho_i / (1 - \zeta)), i = 1, 5 \quad (4.3-10)$$

where ζ is a regression correction parameter, and the ρ_i are parameterizations of the multiple scattering and absorption by the atmosphere, scattering by the cloud, and reflectance by the surface Minnis et al. (1993b). The reflectance parameterization is described briefly below.

The visible-channel reflectance contributed by the cloud and the atmosphere above it is

$$\rho_1 = t_{a1} \rho_{c1} = t_{a1} \rho_{c1}(\tau, \tau_{R1}) \quad (4.3-11a)$$

where the transmittance,

$$t_{a1} = \exp[-\tau_{O_3}(1/\mu_o + 1/\mu)]$$

and the Rayleigh optical depth above the cloud is τ_{R1} . The beam reflectance by the surface is

$$\rho_2 = t_c \downarrow t_c \uparrow \rho_s \quad (4.3-11b)$$

where the downward and upward cloud transmittances are

$$t_c \downarrow = \exp[-(1 - f_D)\tau/\mu_o]$$

and

$$t_c \uparrow = \exp[-(1 - f_D)\tau/\mu]$$

respectively, and f_D is the fraction of the beam that is forward scattered because of diffraction or direct transmission through the droplet or crystal. Its value is generally greater than or equal to 0.5 at visible wavelengths. The proportion of the radiation that is scattered out of the forward direction, reflected by the surface, and transmitted diffusely back through the cloud to space is approximated as

$$\rho_3 = \alpha_{sd}(1 - \alpha_{cd})(1 - t_c \uparrow - \alpha_c) \quad (4.3-11c)$$

The fourth term,

$$\rho_4 = \left[\rho_{R2}(1 - \alpha_c^{0.5}) - \alpha_{R1}\alpha_c^2 \right] (1 - \alpha_{cd}) \quad (4.3-11d)$$

accounts for the relative thickness of the Rayleigh layers above and below the cloud. The effects of the two Rayleigh layers are included by using the direct Rayleigh reflectance term for the bottom layer, ρ_{R2} , and the Rayleigh albedo for the top layer, α_{R1} . The fifth term,

$$\rho_5 = a_0 + a_1 \left(\frac{\tau}{1 + \tau^2} \right)^2 \mu_o^2 \alpha_s + a_2 \alpha_{sd} \quad (4.3-11e)$$

accounts for an overestimate in the surface contribution to the reflectance by ρ_2 for small cloud optical depths. The coefficients, a_i , depend on the microphysical model. The denominator in (4.3-11) uses the parameter

$$\zeta = b_0 + b_1 \ln \tau + b_2 \alpha_{sd} \ln \tau + b_3 \alpha_{sd} \quad (4.3-12)$$

to minimize biases in the parameterization. The coefficients, b_i , also vary with the microphysical model. Details of this parameterization are given by Minnis et al. (1993b).

The model represented by (4.3-11) yields relatively accurate optical depths over dark surfaces for all optical depths (Minnis et al. 1993b). For brighter surfaces, such as deserts, clouds, and snow, the optical depth errors can be greater than 50% for relatively thin clouds. Therefore, the lookup tables for top-of-the-atmosphere reflectance are used if $\alpha_{sd} > 0.20$ and $\tau \leq 8$. The lookup table values are first multiplied by t_{a1} to account for ozone variability and then interpolated to obtain the top-of-the-atmosphere reflectances corresponding to the observed or expected clear-sky albedo and the specified cloud and angular conditions. These values replace the results of (4.3-11) for the thin clouds over bright scenes.

The three equations (4.3-4), (4.3-6), and (4.3-11) are solved using the iterative process outlined in Figure 4.3-10 for each cloudy pixel. An initial guess solves (4.3-11) for τ assuming a water-droplet model with $r_e = 8 \mu\text{m}$. Cloud emittance is computed for channels 3 and 4 using (4.3-9); T_{cld} is then determined from (4.3-4) at $11 \mu\text{m}$. If $T_{cld} > 253 \text{ K}$, then it is used in (4.3-6) with τ to compute $BTD_{3-4}(r_e)$ for the full range of particle sizes in the water droplet model. Otherwise, $BTD_{3-4}(D_e)$ is calculated for the ice crystal models. Finally, a new estimate of particle radius, r_e' , or D_e' , is determined by matching the observed BTD_{3-4} with the model output. For the water droplet case, if BTD_{3-4} is less than the value of the greatest model radius and $T_{cld} < 273 \text{ K}$, the process is repeated using the ice crystal models beginning with an initial guess of $D_e = 37 \mu\text{m}$. Otherwise, r_e is set equal to r_e' and the process is repeated until the two values are within $0.1 \mu\text{m}$ of each other. Likewise, in the ice crystal case, if $T_{cld} > 233 \text{ K}$ and BTD_{3-4} is greater than that of the smallest ice crystal model, the process is repeated using the water droplet models. The test for phase is executed only after the first iteration. An additional 10 iterations are allowed before the process is ended and no solution is obtained. Most cases require fewer than six iterations. In some instances, the ice and water droplet models will produce overlapping results so that the small ice crystals may occasionally be mistakenly identified as large water droplets. Overlapped cirrus and liquid water clouds and mixed-phase clouds can produce radiances that fall between the ice and liquid models.

This approach is illustrated using 1-km AVHRR data taken near Coffeyville, Kansas during the November-December 1991 FIRE Cirrus field experiment. Figure 4.3-11(a) plots the observed BTD_{3-4} against T_4 for a small area at 1900 UTC, November 22, 1991. The plotted numerals correspond to the number of pixels having the given pair of BTD_{3-4} - T_4 values. The curves represent the ice and water droplet model results for $T_{cld} = 264 \text{ K}$. Figure 4.3-11(b) is a histogram of r_e derived using the process described above for the data in Figure 4.3-11(a). In this case, the cloud is diagnosed as being a

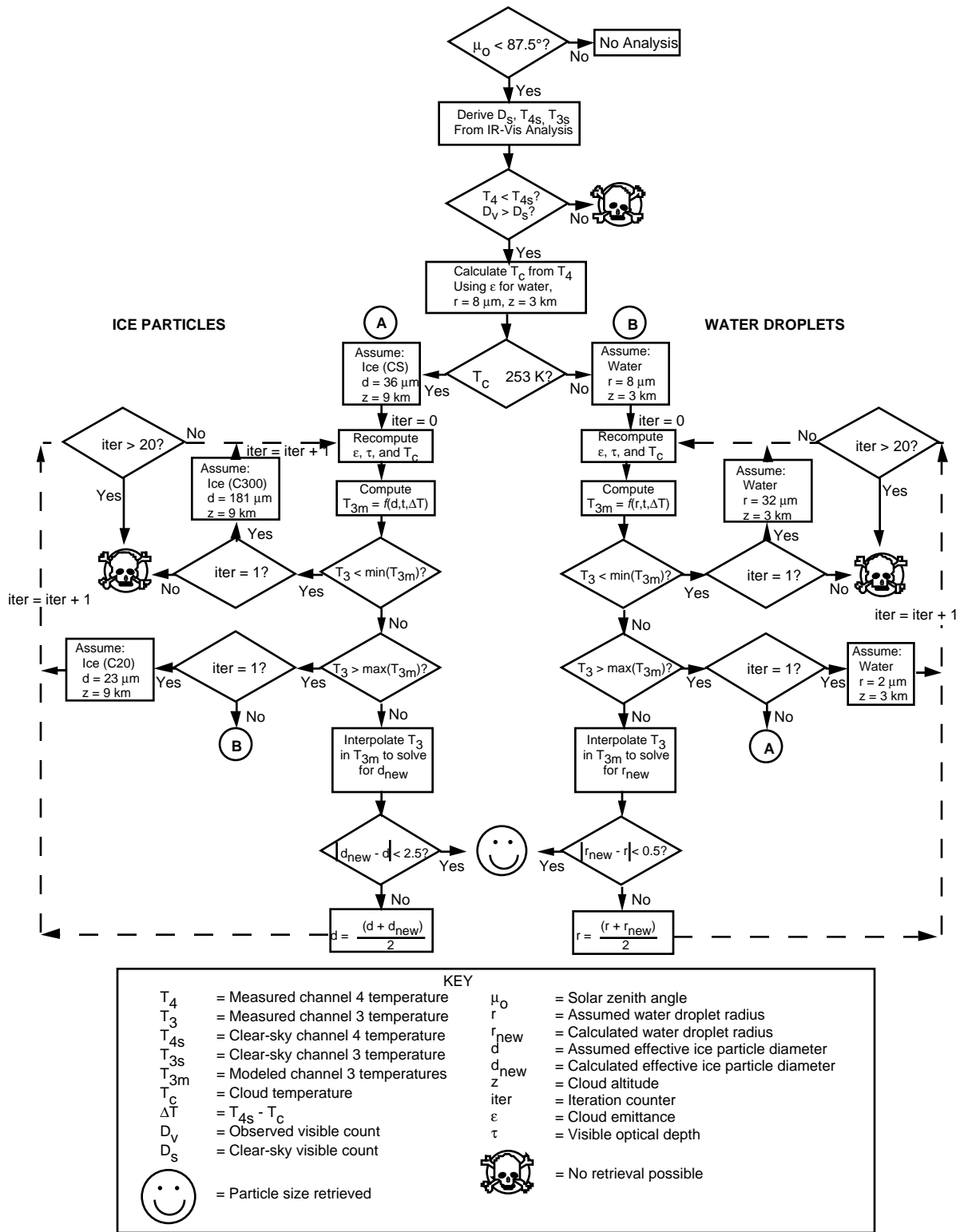
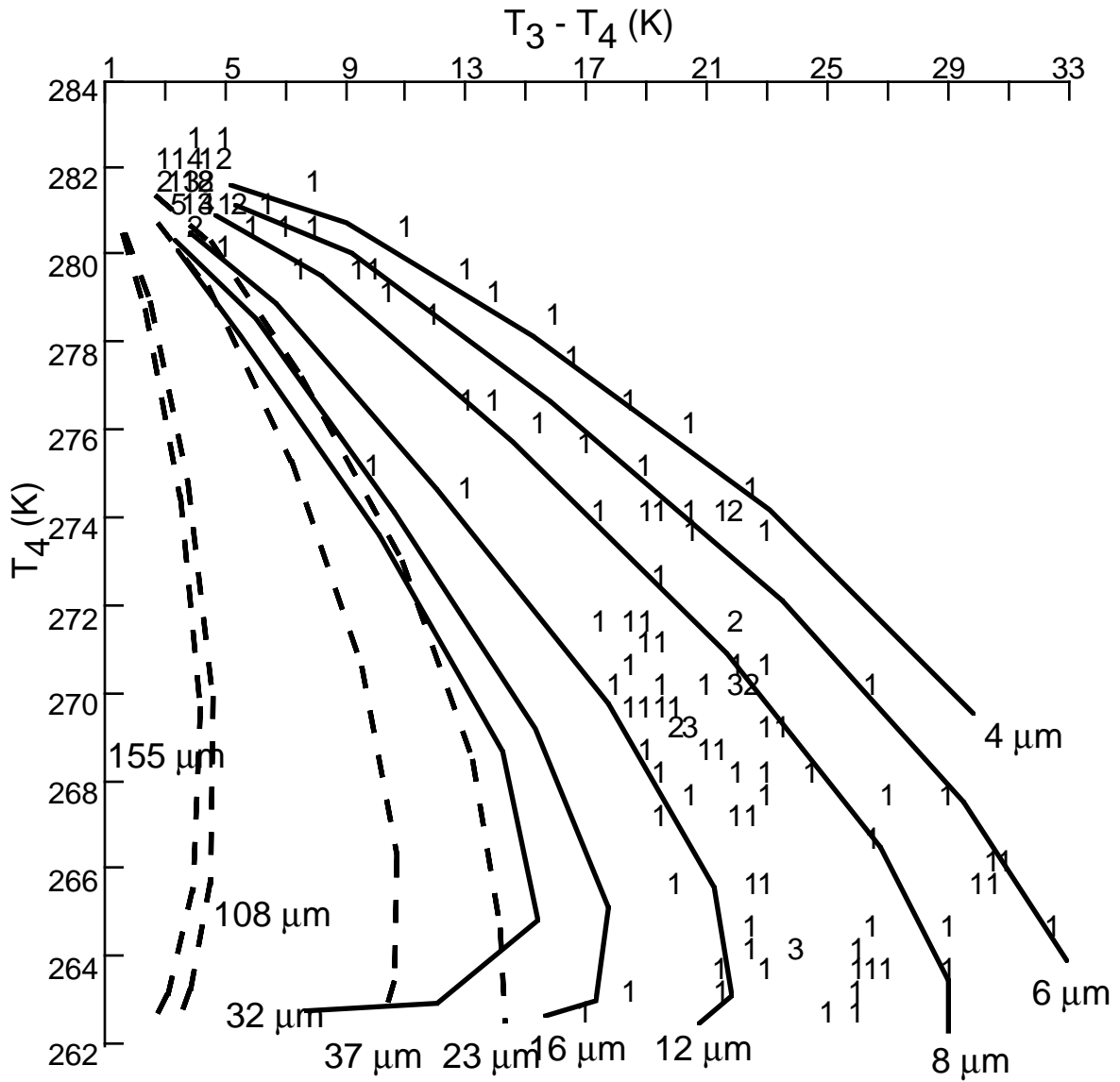
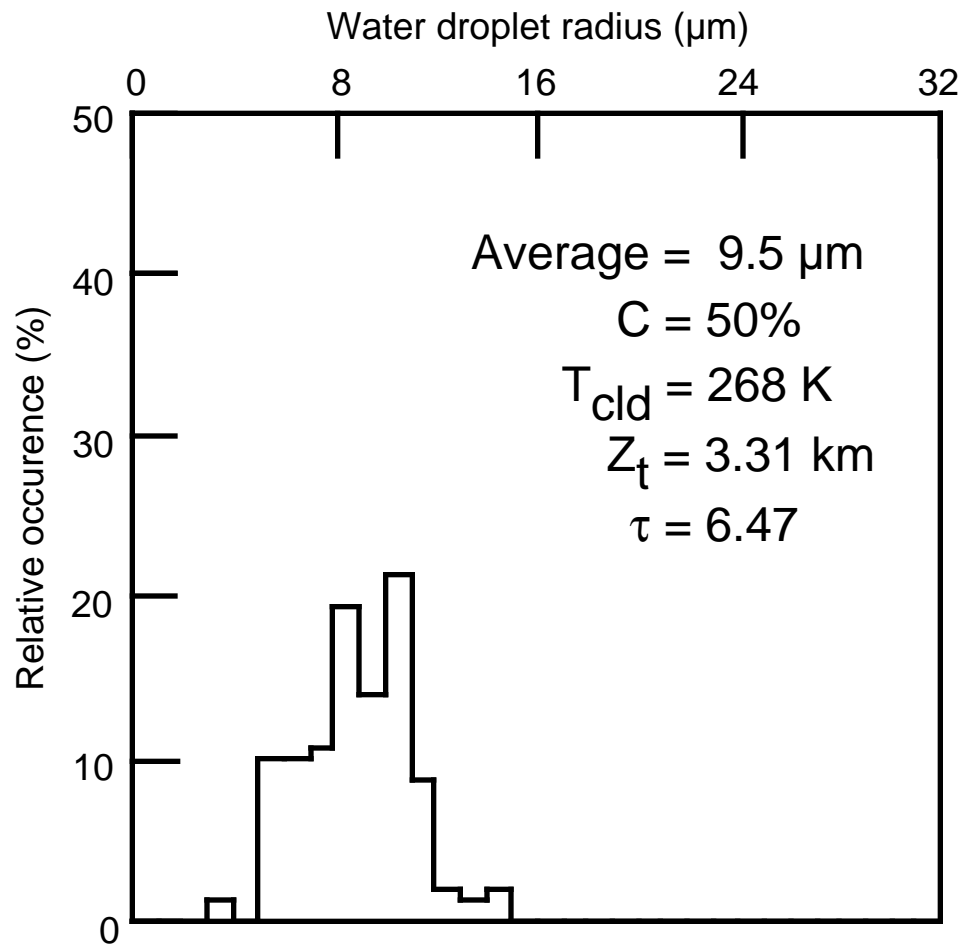


Figure 4.3-10. Flow diagram of channels 1, 3, and 4 cloud property retrieval algorithm. Effective diameter is denoted with d ; effective radius is r .



(a) Observed $BT_{D_{3-4}}$ plotted against T_4 .

Figure 4.3-11. AVHRR BT_{D-IR} histogram and water cloud retrieval in AVHRR data over 39.3°N, 98.1°W at 2054 UTC, November 26, 1991.



(b) Histogram of r_e .

Figure 4.3-11. Concluded.

supercooled water cloud with mean r_e , τ , and T_{cld} values of 9.5 μm , 6.5, and 268 K, respectively. A case where nonoverlapped high- and low-level clouds are present is shown in Figure 4.3-12 for data taken at 2042 UTC, November 28, 1991. The figure shows two-dimensional histograms of ρ_{vis} versus T_4 (Fig. 4.3-12(a)) and BTD_{3-4} versus T_4 (Fig. 4.3-12(b)) with a subjective estimate of the model that would best fit the histograms using the LBTM-derived (section 4.2.2.) values of T_{cld} from Figure 4.3-12(a). The full pixel-by-pixel analyses yielded the distribution of particle sizes given in Figure 4.3-13. The low-cloud top height of 1.6 km is 0.2 km higher than that derived from radar data taken at Coffeyville. The high-cloud altitude is at 9.0 km, midway between the base and top heights observed with the radar. The ice water path of the cirrus cloud is

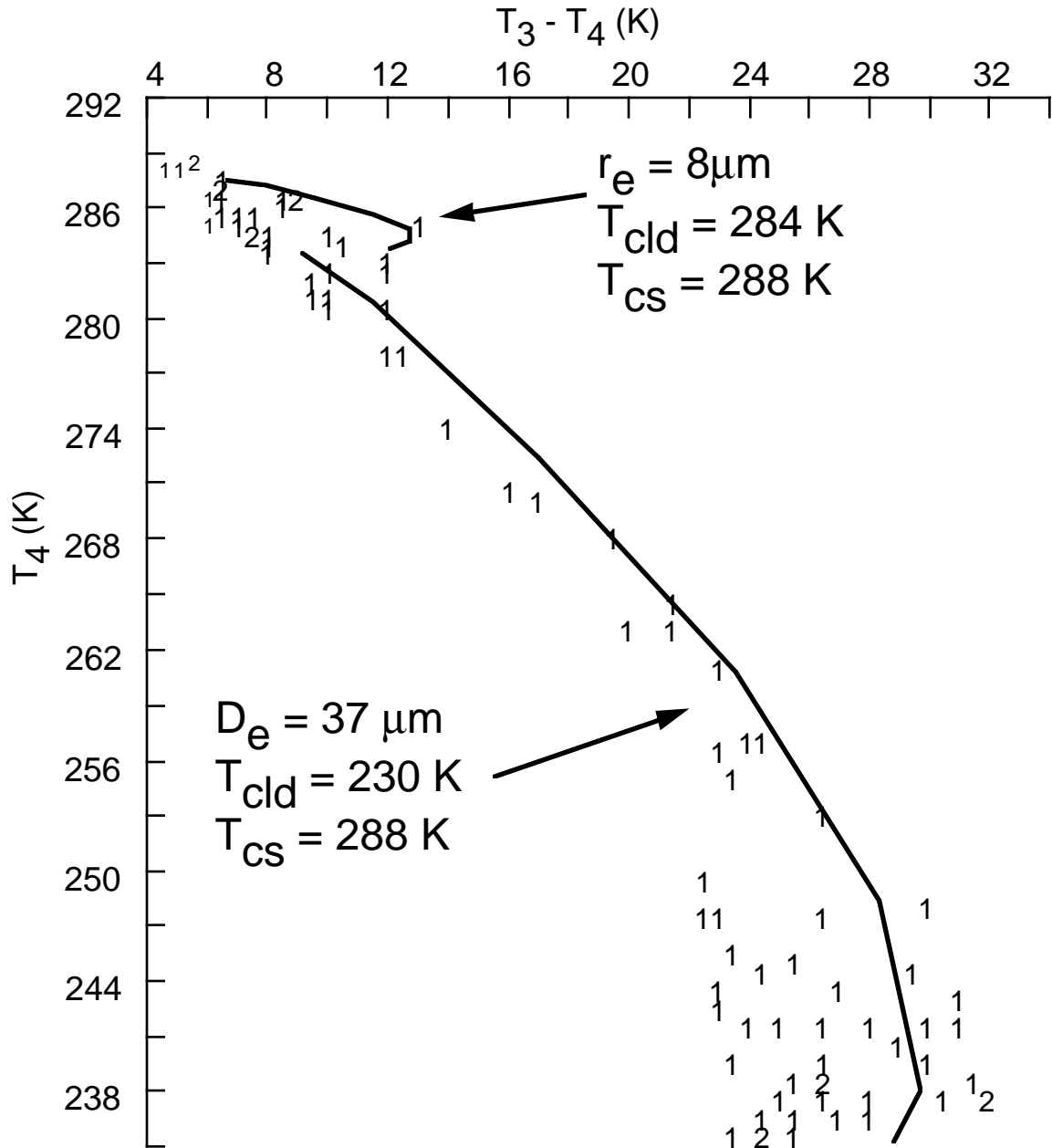
$$W_{ice} = \delta_{ice} \Sigma(V_i N_{oi}) \tau / \Sigma 2A_i N_{oi} \quad (4.3-13)$$

where V and A are the volume and cross-sectional areas, respectively, of the randomly oriented hexagonal crystal i in a specified distribution defined by the normalized number of crystals N_o , and δ_{ice} is the density of ice. The ice water path derived from the distribution in Figure 4.3-13(b) is 132 gm^{-2} a value within 5% of the 139 gm^{-2} derived from the surface radar. This result indicates the mean particle size is a reasonable estimate for the cloud. The high-cloud fraction is reduced from the LBTM analysis (Fig. 4.3-12(a)) because the cloud pixels with $T_4 > 276$ K were too dim in the visible channel to solve for τ and r_e . The mean value of r_e in Figure 4.3-13(a) yields $W_{liq} = 47 \text{ gm}^{-2}$, a value twice that of the half-hour-long surface microwave measurement; but it was derived using only four pixels or ~ 10 minutes. Evaluation of a larger area of nearby low clouds provides a more appropriate comparison because it represents a longer time interval and the scene contains only one cloud layer. The results are $r_e = 11.9 \mu\text{m}$ and $W_{liq} = 30 \text{ gm}^{-2}$. Comparisons of data taken during the FIRE II cirrus experiment found that the satellite-derived particle sizes from this method were within 15% of coincident ground-based, radar-derived ice particle sizes. These initial validations indicate that this technique can yield relatively accurate estimates of particle size and liquid water path.

Another example (Fig. 4.3-14) taken from AVHRR data near Coffeyville shows the difficulties arising from overlapped clouds. Here the retrieval for overlapped cirrus and low stratus yields large water droplets $r_e = 16 \mu\text{m}$ and clouds at 4.0 km (Fig. 4.3-15(a)) in addition to the high clouds at 7.4 km with $D_e = 58 \mu\text{m}$ (Fig. 4.3-15(b)). Nearby analyses of single layer stratus and cirrus yielded $r_e = 10 \mu\text{m}$ and $D_e = 46 \mu\text{m}$, respectively. The surface instruments and soundings showed no indication of clouds in the middle layers but did show the two layers. Some of the clouds are apparently nonoverlapped because there are peaks in the size distributions at $r_e = 10 \mu\text{m}$ (Fig. 4.3-15(a)) and at $D_e = 40 \mu\text{m}$ (Fig. 4.3-15(b)). The overlapped clouds yield overestimates of particle size. This example shows that without knowledge of the overlap, the method will return errant values of T_{cld} and r_e for cases involving an optically thin cirrus over a lower cloud.

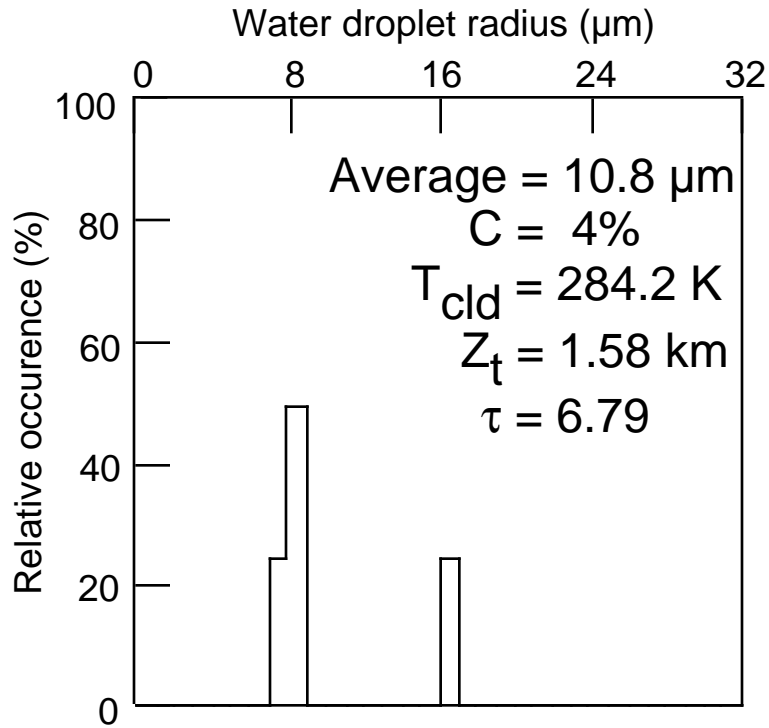
4.3.4.1.2. Reflectance technique. The reflectance approach uses the ratio $\rho_{0.65}/\rho_{1.65}$ to determine the phase of the clouds by comparing the ratio to model calculations for thick ice and water droplet clouds. For each single-layer pixel, the phase will be determined by comparing the reflectance ratio to an ice-water threshold computed for μ_o , μ , and ϕ using the models discussed earlier. If the ratio exceeds the greatest model ice ratio, the cloud will be designated as liquid water; otherwise, the phase is ice.

After determination of the phase, a least squares approach is applied to match the multispectral radiances to a set of model calculations simulating the reflectances for clouds having a range of particle sizes and optical depths. This approach, the models to apply it, the expected errors, and current limitations are discussed in detail by King and Tsay (1993). This technique will use the VIRS 0.65-, 3.75-, and 1.60- μm data during CERES/TRMM. It is anticipated that CERES/EOS will use the 3-channel reflectance method employing the 2.13- μm MODIS channel. In the Release 2 software design for the COPRS, the reflectance method may serve as the primary particle size retrieval method.

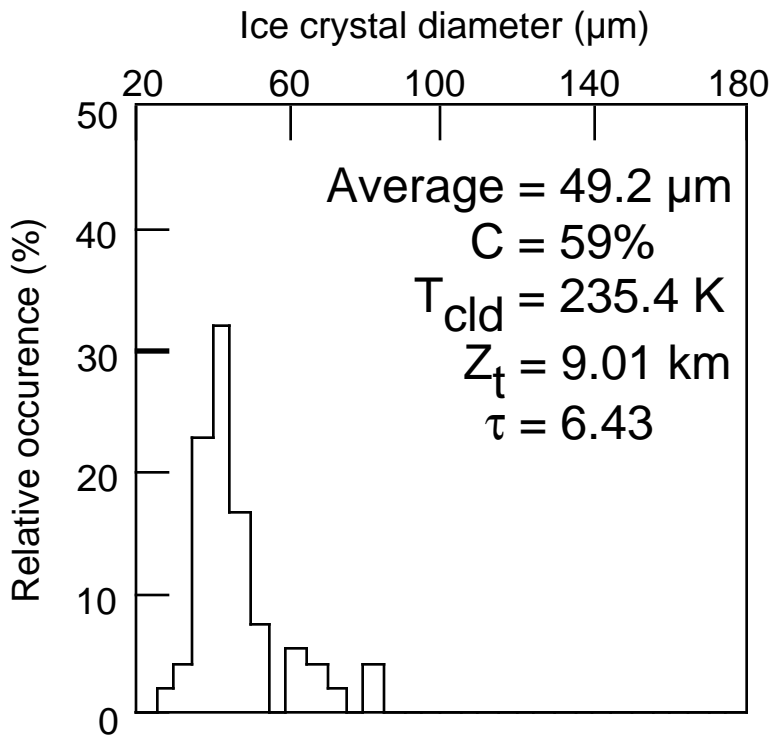


(b) BTD-IR histogram.

Figure 4.3-12. Concluded.



(a) Water cloud retrieval.



(b) Ice cloud retrieval.

Figure 4.3-13. Retrieval in AVHRR data over 37.3°N, 95.1°W at 2042 UTC, November 28, 1991.

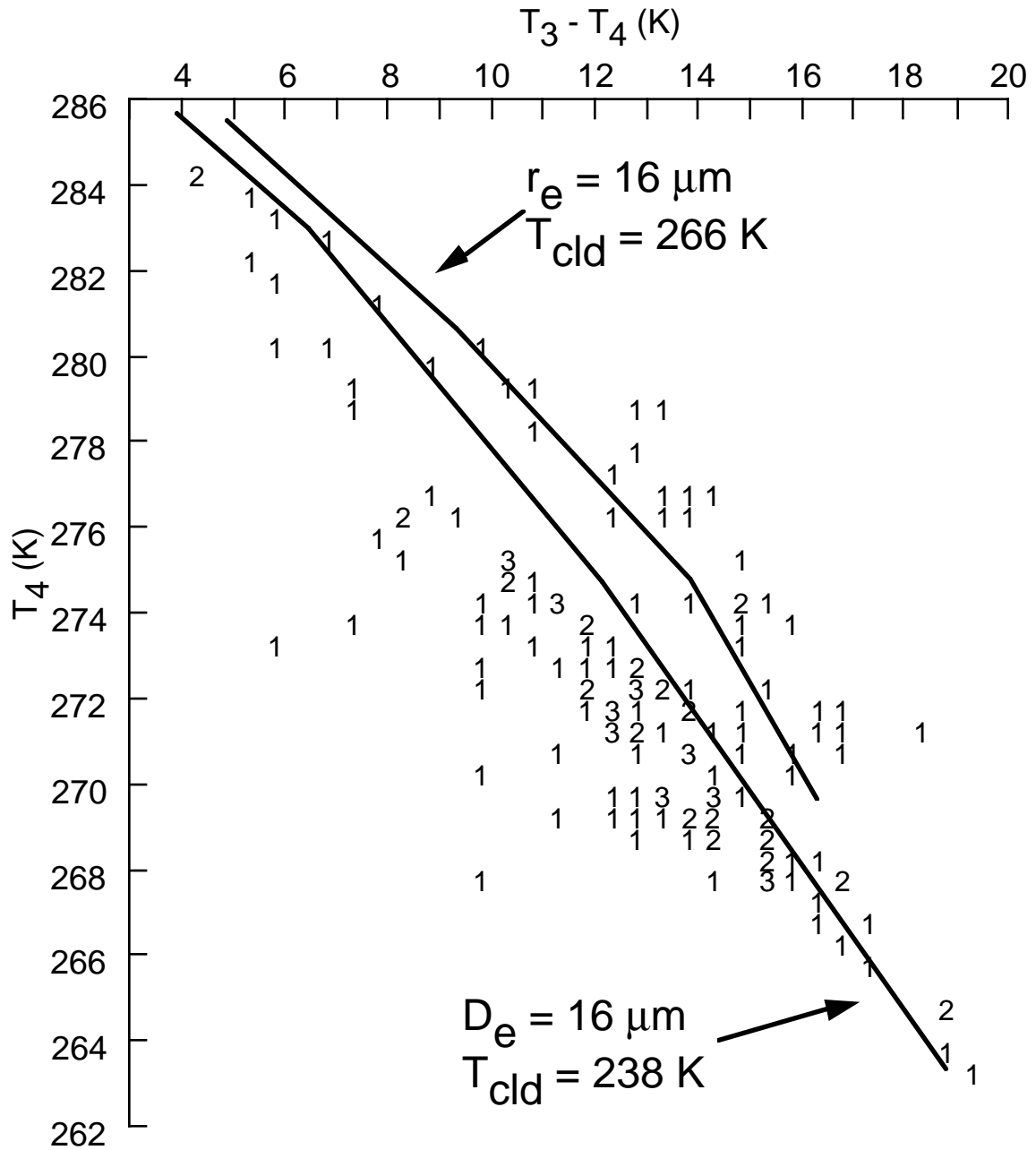
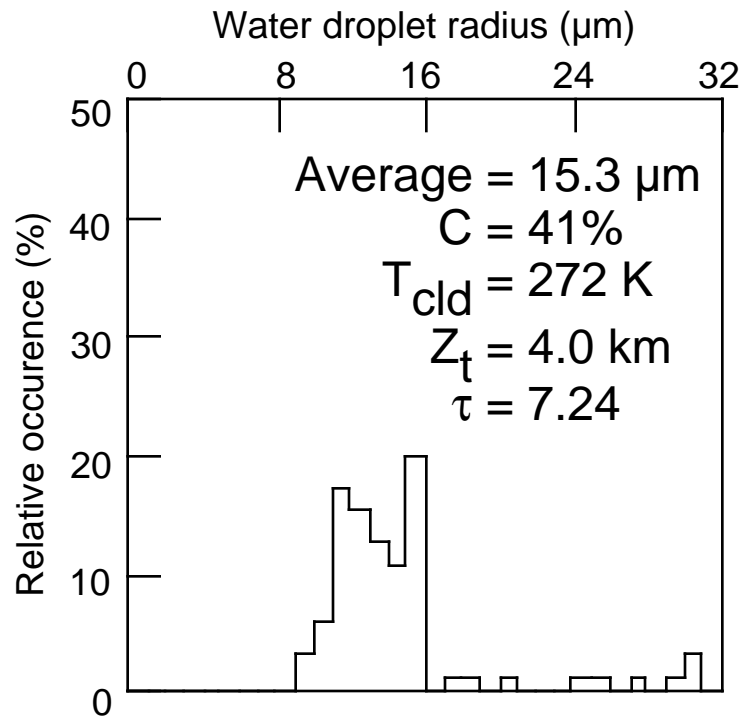
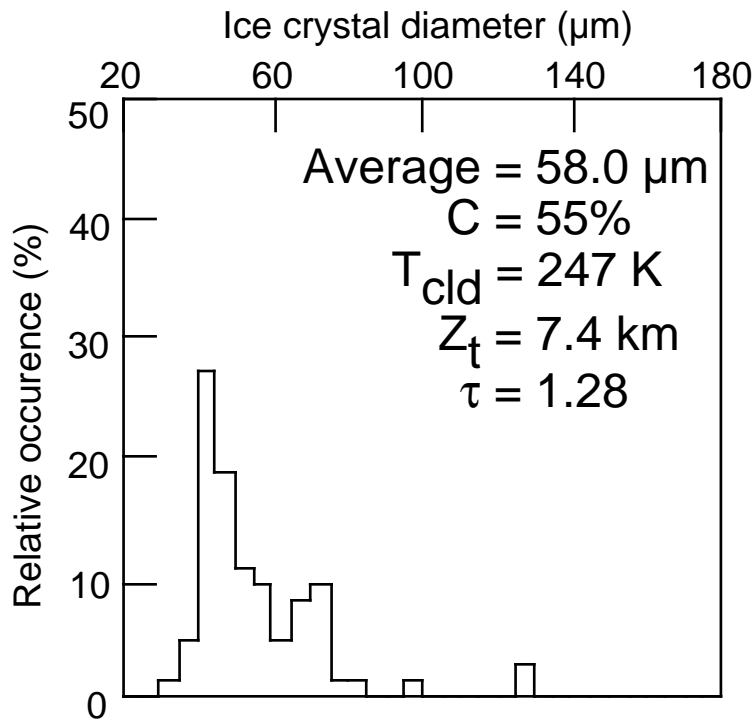


Figure 4.3-14. AVHRR BTD-IR histogram over 37.1°N, 95.6°W at 2036 UTC, November 28, 1991.



(a) Water cloud retrieval.



(b) Ice cloud retrieval.

Figure 4.3-15. Retrieval in AVHRR data over 37.1°N, 95.6°W at 2036 UTC, November 28, 1991.

4.3.4.2. Nighttime Cloud Optical Depth, Particle Size, and Cloud Temperature

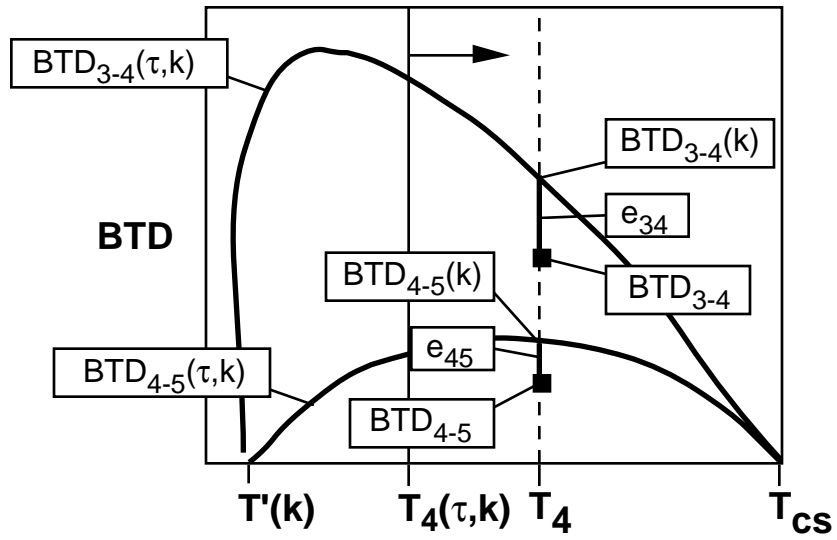
The cumulative experience of remotely sensing particle size and optical depth at night is much less than that for the daytime. The available techniques are either in early development or in a conceptual stage at this time. The primary shortcoming to the nocturnal methods is the lack of a relatively independent optical depth channel. When the sun is shining, it is usually possible to obtain a close approximation of optical depth using the visible channel because of its relative insensitivity to particle size (Fig. 4.3-6) and its independence from T_{cld} . This facilitates the determination of T_{cld} and, ultimately, r_e . At night, the problem is less tractable because all three channels are highly sensitive to T_{cld} and τ for small optical depths ($\tau < 6$). Although T_{cld} is well defined for larger optical depths, there is minimal information available regarding τ and r_e . For those clouds having small optical depths, particle size and τ can be determined using one of the approaches described below.

4.3.4.2.1. Iteration-interpolation. Given an optically thin cloud ($\tau < 6$), μ , and the background (clear-sky or cloudy) temperatures for channels 3, 4, and 5, it is assumed that a given pair of BTD_{3-4} and BTD_{4-5} at a particular value of T_4 uniquely define a cloud characterized by T_{cld} , r_e or D_e , and τ . These parameters can be determined by matching the three measured quantities as closely as possible to the same parameters calculated using each of the microphysical models defined for the COPRS. Each observed quantity will fall between the corresponding pair of discrete theoretical calculations for a given phase. The distance in BTD from the model value to the observed value is used to interpolate between each model for each parameter to assign a value of cloud temperature, optical depth, and particle size to the pixel for both channels 3 and 5. In the absence of temperature indications, the phase is selected based on how closely the channel 3 and 5 parameters agree with each other. The final values of T_{cld} , r_e or D_e , and τ are determined by averaging the channels 3 and 5 results for the selected phase.

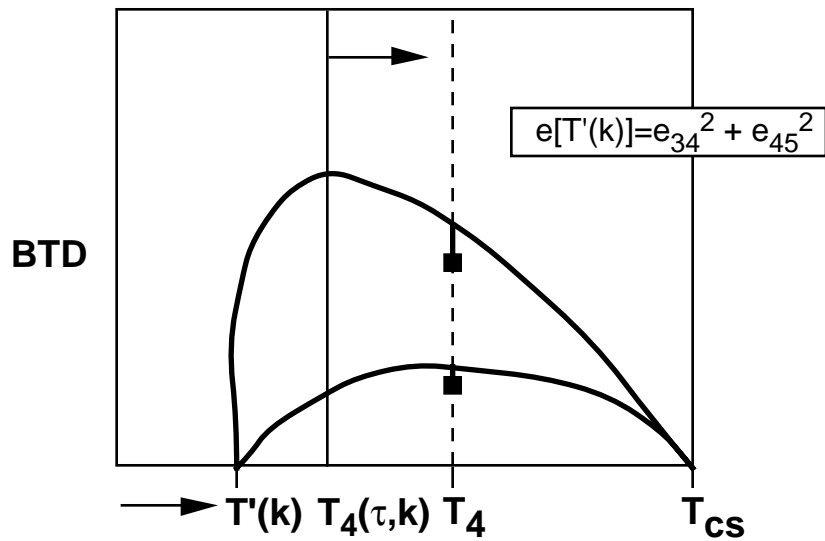
This technique attempts to determine τ , T_{cld} , and particle size through an iterative process that minimizes the differences between model-derived and observed values of BTD_{3-4} and BTD_{4-5} for the observed T_4 . This procedure, illustrated schematically in Figure 4.3-16, begins with values given for μ and T_{cs} and assumes an initial value of $T_{cld} = T'(k)$, where $T'(k) < T_4$ and k is an emittance model index corresponding to a particular particle size and phase. The tropopause temperature is the initial value of T_{cld} unless the layer analysis (section 4.2.) indicates only a single layer is present or $BTD_{3-4} < BTD_{3-4cs}$. In the former case, the initial cloud temperature is the layer temperature minus 5 K. If $BTD_{3-4} < BTD_{3-4cs}$, the starting temperature is $T_4 - 5$ K. For each of the channel-4 emittance models (4.3-8), $\tau[T'(k), k]$ is determined using a secant iteration method to match T_4 . This process is represented by the arrow in Figure 4.3-16(a). The resulting value of τ is used to compute T_3 and T_5 using the channels 3 and 5 emittance models in (4.3-4). The model values of $BTD_{3-4}[T'(k), k]$ and $BTD_{4-5}[T'(k), k]$, shown as the intersections of the model curves and the dashed line in Figure 4.3-15(a), are calculated from the model-derived temperatures and the observed T_4 . Difference errors, $e_{34} = BTD_{3-4} - BTD_{3-4}[T'(k), k]$ and $e_{45} = BTD_{4-5} - BTD_{4-5}[T'(k), k]$, are computed for each model. A composite error,

$$e[T'(k), k] = e_{34}^2 + e_{45}^2 \quad (4.3-14)$$

becomes the parameter to minimize. These operations are repeated varying $T'(k)$ as illustrated in Figure 4.3-16(b) until $e(T_{new}, r_e)$ is minimized yielding the best estimate of cloud temperature for model k . In the first iteration, $T'(k)$ is increased by 10 K for each step until e begins to increase. Figure 4.3-17(a) depicts how e can vary with increasing $T'(k)$. Subsequent iterations repeat the error calculations using increasingly smaller temperature increments bounded by the last two temperatures used in the preceding iteration. The iterations continue until the increment is less than 0.1 K. For the case in Figure 4.3-17(a), the value of $T_{cld}(k)$ corresponds to the minimum error. This entire procedure is repeated again for each model producing final values of $e[T'(k), k]$ as shown in Figure 4.3-17(b). In practice, the algorithm begins with the smallest model for the phase and continues until e_{34} and e_{45}

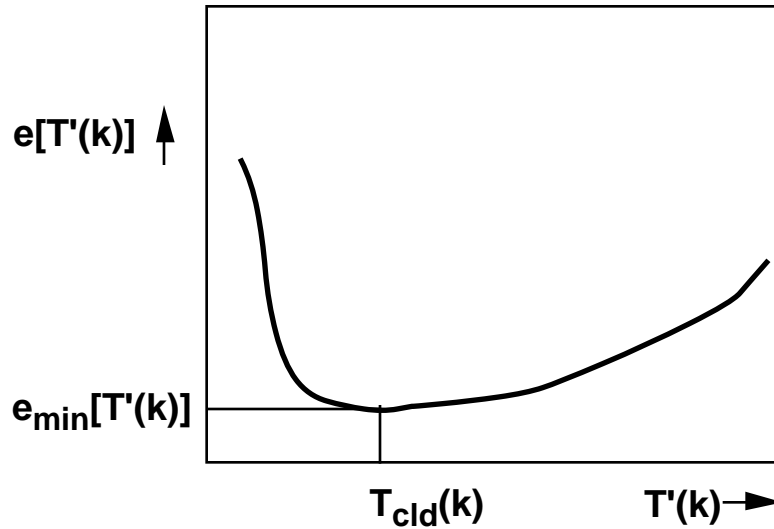


(a) First step of iteration process; compute errors for model k using first guess temperature.

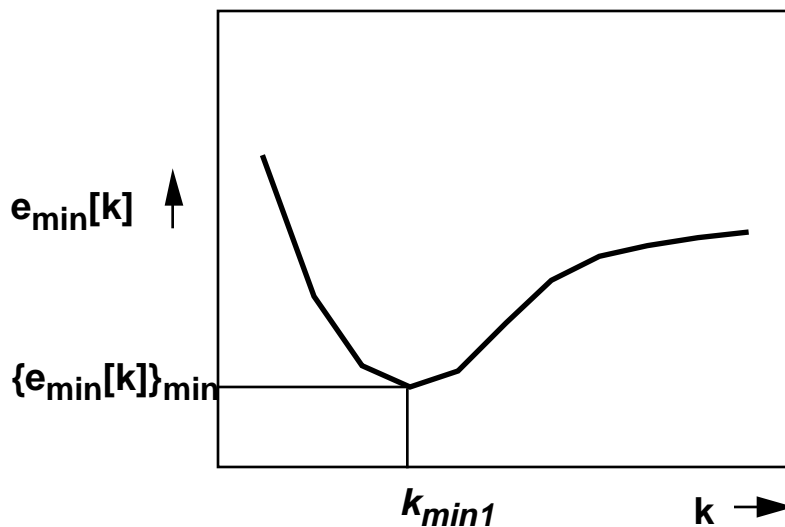


(b) Second step of iteration process; compute errors for second cloud-temperature guess.

Figure 4.3-16. Schematic illustration of emittance iteration process for nighttime cloud property retrievals.



(a) Determination of the minimum error in a given particle size model.



(b) Determination of model having minimum error.

Figure 4.3-17. Schematic diagram of minimum error estimation to determine most appropriate particle size models.

switch signs. The sign change in these error values indicates that the observation is between the last two models. One of the two models, k_{min1} , will have the smallest value of e for the particular phase, while the other model, k_{min2} , should also have a relatively low error. These two models are then selected for interpolation. If $T_{cld} > 273$ K, only the water-droplet models are used. Conversely, if $T_{cld} < 233$ K, only the ice-crystal models are considered further.

Final values of r_e or D_e , T_{cld} , and τ are computed for channel 3 by linearly interpolating between $r_e(k_{min1})$ and $r_e(k_{min2})$, $T_{cld}(k_{min1})$ and $T_{cld}(k_{min2})$, and $\tau(k_{min1})$ and $\tau(k_{min2})$, respectively, using $e_{34}[T'(k_{min1}), k_{min1}]$ and $e_{34}[T'(k_{min2}), k_{min2}]$ as the independent variables. The same interpolation is repeated for channel 5. The resultant values for the two channels are averaged to obtain the best estimate

of each parameter. If both phases are considered, then the results for the phase having the smallest uncertainty,

$$e_{35} = \left(\frac{T_{cld3} - T_{cld5}}{T_{cld3}} \right)^2 + \left(\frac{\tau_3 - \tau_5}{\tau_3} \right)^2 + \left(\frac{r_{e3} - r_{e5}}{r_{e3}} \right)^2 \quad (4.3-15)$$

are selected for the final parameter values. The subscripts 3 and 5 refer to the parameter values derived using channel 4 with channels 3 and 5, respectively. The most accurate estimates of T_{cld} are obtained for the larger optical depths ($\tau > 6$), while the most accurate values of τ and r_e should occur for ($1 < \tau < 6$). There is little variation in BTD with particle size for small and large optical depths. This method was tested using a limited set of simulated data with superimposed noise. In these cases, the retrieved particle sizes were within $0.1 \mu\text{m}$ of the simulated cloud values and the phase was chosen correctly. Testing of this method with actual data is underway.

4.3.4.2.2. Single-layer, fixed-size technique. An alternate method that may be included in the COPRS is the technique of Lin and Coakley (1993) that interprets the pixel radiances for a single-layer cloud deck as

$$B(T) = (1 - C)B(T_{cs}) + C(\epsilon B(T_{cld}) + tB(T_{cld})) \quad (4.3-16)$$

where wavelength is implied and C and ϵ are the pixel-scale fractional cloud cover and cloud emittance, respectively. The cloud temperature and particle size index are determined iteratively from the group of pixels constituting the cloud deck. The emittance models described earlier will be used to determine particle size and phase. A single cloud temperature and effective radius are assumed for the entire deck. Those two parameters define a set of solutions to (4.3-16) that envelope most of the pixels representing the cloud deck. The emittance and cloud fraction for each pixel within the envelope are obtained through simultaneous solution of (4.3-16) for channels 4 and 5. Details of this method are given by Lin and Coakley (1993).

This technique is limited to those conditions where a single layer is easily discernible. It allows no variation of particle size and radiating temperature within the deck. The particle size derived for the deck tends to be the smallest observable particle size for the given set of pixels because it is defined by those pixels essentially having the greatest BTD_{4-5} for a given T_4 . The cloud temperature also tends to be the coldest observed brightness temperature. This method, however, requires no iteration and is relatively simple to implement. Refinement of the technique is continuing.

4.3.4.3. Multiple Cloud Layer Retrievals

The discussion above generally applies to single layer clouds or to overlapped clouds that include an optically thick upper cloud layer. In either case, the pixel index will probably denote a single layer cloud. For data blocks with multiple cloud layer pixels, a slightly different approach is taken. The first step for a given data block is to determine the particle sizes for all of the single-layer pixels. When available, the mean particle sizes and temperatures are computed for each layer. If single-layer particle size is not available, only the layer temperatures are available from the subsystem input dataset. Two approaches are taken for these cases.

When the layer temperatures and particle sizes are available, optical depth is the remaining unknown quantity if the background temperature is specified. In the case of multiple layers, the background temperature may vary with the emittance or optical depth of the lower cloud. The range of the background temperature is simply $T_{cs} - T_{lc}$, where T_{lc} is the lower-cloud temperature. An envelope of T_4 and BTD_{3-4} can be constructed using the upper cloud temperature T_{uc} as T_{cld} , and T_{lc} and T_{cs} as the temperatures used to compute the clear radiance term in (4.3-4) and (4.3-9). Multilevel pixels falling outside this envelope will be treated as single-layer pixels and the particle size and cloud temperature

retrieval will be executed in the normal fashion. Those pixels with values within the envelope will be analyzed for particle size and background or “clear-sky” temperature. The initial background temperature is found by linear interpolation between the lower and upper bounds of BTD_{3-4} at the observed T_4 . The optical depth of the upper cloud is found using (4.3-4). The final values of the lower and upper cloud optical depths are found by iterating this process. The mean particle sizes and temperatures for the upper and lower clouds are assigned to all of the pixels in the envelope.

When layer temperatures are the only parameters available, it is assumed that the lower cloud is optically thick so that T_{lc} is the only value substituting for T_{cs} . The 3-channel infrared method is then applied to find optical depth and cloud particle size. If particle sizes can be retrieved, they are used to compute mean values for the upper layer. The first approach is then invoked for the remaining pixels if they are available. If no particle sizes are retrieved, the particle size is specified using default values for water and ice. Optical depths are then computed using the visible reflectance. A technique for using the MODIS 1.38- μm channel will also be explored for estimating the high cloud optical depth. The methods for processing multilayer pixels are in the development stage.

4.3.4.4. Water Path

Rearranging (4.3-7) gives the liquid water path,

$$W_{liq} = \frac{4\delta_{liq}r_e\tau}{3Q_e} \quad (4.3-17)$$

for a given effective droplet radius and optical depth. Using the model distributions in (4.3-13) in a regression fit yields the ice water path,

$$W_{ice} = \delta_{liq}\tau D_e(0.304 + 0.00124D_e) \quad (4.3-18)$$

for the retrieved ice-crystal size and optical depth.

4.3.4.5. Cloud Top and Base Altitudes

Cloud-top height Z_t is the lowest altitude from the sounding corresponding to T_{cld} . Because the value of T_{cld} may correspond more closely to the center of the cloud in optically thin cases, it will be adjusted in some cases to account for semitransparency. The adjustment uses the approach of Minnis et al. (1990a) for cirrus clouds. The channel-4 cloud-top emittance is defined as

$$\epsilon_t = \epsilon_4(2.97 - 0.00914T_{cld}) \quad (4.3-19)$$

The cloud-top temperature T_t is computed using the observed value of T_4 and T_{cs4} in (4.3-4). This approach is used only for $T_{cld} < 253$ K. For warmer clouds, $\epsilon_t = 0.98\epsilon_4$. No adjustment is made for water clouds because the correction is usually less than 0.1 km, the precision of the height determination. Cloud base is given as $Z_b = Z_t - \Delta Z$. The cloud thickness ΔZ is computed using empirical formulae. For clouds below 4 km, $\Delta Z = 0.08\tau^{1/2} - 0.04$ (Minnis et al. 1992). When $\Delta Z < 0.02$ km, ΔZ is set to 0.02 km. For other clouds,

$$\Delta Z = 7.5 - 0.026T_c + 0.85 \ln \tau \quad (4.3-20)$$

(Smith et al. 1993). The minimum thickness for these clouds is also 0.02 km, with a maximum of 8 km. Cloud base and top pressures correspond to Z_b and Z_t in the vertical profiles of $Z(p)$ and $T(p)$.

4.3.5. Practical Considerations

4.3.5.1. Computer Requirements

4.3.5.1.1. Model input. The bidirectional reflectance models have been computed for 13 particle sizes. They are discretized at 12 optical depths. The last four optical depths are not included for the 3.75- μm channel since the reflectance is essentially invariant for larger optical depths. The arrays for each particle size require 0.25, 0.25, and 0.19 megabytes of storage, respectively, for the 0.65-, 1.61-, and 3.75- μm channels. The emittance models for each particle size have been computed for 3.75, 11, and 12 μm . A total of 75 coefficients are used for each emittance model.

4.3.5.1.2. Subsystem output. The output comprises a set of 16-bit integer values that define the cloud properties for each pixel in the analysis block. The parameters are phase (dimensionless), particle size (units of $\mu\text{m} \times 10$), cloud visible optical depth (dimensionless $\times 10$), channel-4 zenith emittance (dimensionless $\times 100$), cloud liquid or ice water path ($\text{kg}/\text{m}^2 \times 1000$), cloud-top pressure (hPa), cloud effective pressure or $p(T_{\text{cld}})$ (hPa), cloud-base pressure (hPa), cloud effective temperature ($\text{K} \times 10$), cloud effective altitude ($\text{km} \times 10$), and cloud effective cloud particle size ($\mu\text{m} \times 10$). In addition, there will be a quality flag and methodology flag to indicate the uncertainty and source of the retrieval for each pixel.

4.3.5.1.3. Data processing requirements. The processing requirements for the reflectance method are given by King and Tsay (1993). The processing needs for the other algorithms are substantial and will be determined.

4.3.5.2. Strategic Concerns

There are many situations that can prevent or diminish the accuracy of a given parameter retrieval. Some situations can be handled through the application of alternative methods, others by using default options. Solutions to all of the problems noted below, as well as others that will inevitably arise in the development of this global methodology, will be examined in current and future research.

4.3.5.2.1. Potential problems. There are many situations that can foil the algorithms outlined above. A listing of all such conditions would be superfluous. Some of the more important potential problems confronting the COPRS are noted below.

In most daytime cases, a reliable retrieval of cloud optical depth, particle size, and temperature can be obtained for optically thick clouds. However, thick low or midlevel clouds can be shadowed by nearby high clouds voiding the plane-parallel assumption in all retrievals using solar reflectance. Shadows also can affect thin-cloud retrievals in variable thickness, single-layer fields (Minnis et al. 1990b). Clouds affected by shadows frequently are darker than the clear-sky pixels so that their properties cannot be obtained with reflectance models. Even when optically thick, ice clouds may not produce reflectances that conform to the model configurations because of the wide variety and potential orientations of the particles in cirrus clouds. Particle size retrievals for clouds containing very large particles will be constrained because of the limited sensitivity of the mixed and emittance methods.

Thin-cloud properties will be severely diminished in accuracy for pixels taken over relatively bright backgrounds such as desert, snow, or other clouds. It may not be possible to obtain a solution in many of these instances. Thin-cloud retrievals near coastlines will also be subject to errors in the clear-sky radiances because of slight mislocations. All of the retrievals are based on plane-parallel radiative transfer models. Thus, for scattered or broken cloud fields or for clouds with internal variations in their optical properties, there may be significant errors in the retrieval of particle size and optical depth (e.g., Stackhouse and Stephens 1994; Duda et al. 1994). Cloud thickness estimates are based on a limited amount of empirical data so that the global applicability of these formulas is highly uncertain. As discussed earlier,

nocturnal retrievals of τ and r_e are not possible for optically thick clouds. During both day and night, retrievals for overlapped clouds will be much less certain than those for single layer clouds. Near the terminator, the geometry and the atmospheric path lengths diminish the variability in the reflected radiance fields and, essentially, negate the plane-parallel cloud assumption. Retrievals that depend on reflectances become much more uncertain. There is still some solar contamination of the channel-3 radiances at the high solar zenith angles so that an emittance-based retrieval must account for the solar reflectance component which is highly uncertain.

4.3.5.2.2. Solutions. Accounting for these various situations presents a challenge to the development of a comprehensive global analysis system. A first-order solution to the problem of shadowed cloud pixels is to tag them as such and assign them the mean values of the nearest cloud layer. If the shadowing is particularly heavy, it can be assumed that the reflected portion of the channel-3 radiance is negligible. In that case, the 3-channel iteration-interpolation method can be implemented. At this time, there is no technique available for finding ice particle shape and orientation using passive satellite measurements. If no solution can be obtained for a single-layer cloud during the daytime using the mixed technique because the particles are too large, the reflectance method using the 1.61- μm channel will be applied. If no solution is obtained, the pixel particle size will be assigned using either the closest extreme model value or the average of all the adjacent pixels. A similar approach is used for optical depth and cloud temperature.

For thin clouds over bright scenes, it may be necessary to use the iteration-interpolation method since the channel-3 surface albedo is relatively small compared to the visible albedo. Similarly, clouds are much more reflective at visible rather than near-infrared wavelengths. In the bright background instances, the channel-3 solar component will be calculated for each of the models and optical depths. The iteration-interpolation method would proceed as usual. This daytime application of the 3-channel emittance method can also be used to determine the consistency between the day and night cloud property retrievals. The use of the 3-channel emittance technique during the day needs further evaluation.

The difficulties of the near-terminator geometry are less manageable than many of the other problems. It may be possible to assume a particle size and derive the cloud temperature and optical depth using channels 4 and 5. When MODIS is operating, the problem is somewhat mitigated because three thermal window channels will be available. At night, when the optical depth and radius retrievals are limited to $\tau \sim 10$, a default value will be assigned.

4.3.5.3. Calibration and Validation

The derived parameters for each pixel are critically dependent on the absolute calibration of the sensors. Although comprehensive sensitivity studies have not been performed for all of the COPRS algorithm components, some estimates of the dependence of particle size on the channel-3 radiance have been made by Han (1992). For example, he found that a precision of $0.0017 \text{ W}\cdot\text{m}^{-2}\cdot\text{sr}^{-1}$ in the channel 3 radiances translates into uncertainties as low as 2% for $r_e < 20 \mu\text{m}$, $\tau > 3$ and as great as 10% in r_e for $\tau \leq 1$. Similar uncertainties in the channel 3 calibration would probably produce particle size errors of the same magnitude. The filter functions of the channel-3 sensor must also be accurately known to derive an accurate value of the spectral solar constant for the calculation of the solar component of the observed radiances. Further sensitivity studies are needed to evaluate the full impact of calibration on the derived quantities.

Validation efforts before, during, and after the CERES flights are essential to understanding the accuracy of the retrieved quantities. Before the initial launches, datasets taken during FIRE, ASTEX, ARM, and TOGA/COARE will be used to verify the optical depths, particle phases and sizes, water path, and cloud temperatures using the developmental code and substitute satellite (i.e., historical AVHRR and GOES) and aircraft data. After launch, FIRE III, SHEBA, and ARM data will be used to assess the operational algorithms. In situ measurements and active remote sensing of cloud

microphysics are needed to estimate the uncertainties in phase and particle size. During TRMM, the VIRS-derived droplet radii over water may also be compared for consistency to r_e retrieved with the microwave liquid-water-path/visible reflectance approach discussed in section 4.3.2.3. Radar and lidar data from aircraft and surface sites are needed to evaluate the particle sizes, cloud-top and cloud-base temperatures, and the ice water paths. Sunphotometers, radar, and lidar data are needed to verify optical depths. Microwave radiometers are needed to assess liquid water path. Other instruments, such as nephelometers, are needed to ensure that the scattering phase functions used in the model calculations are reasonably accurate. All of these types of instruments should be available in part or in total during each of the noted experiments. High-altitude radiometric measurements using wavelengths similar to VIRS or MODIS are needed for calibration checks and for model validation. The ER-2 MODIS Airborne Simulator and the Multispectral Pushbroom Imaging Radiometer (MPIR) proposed for unmanned aircraft by the DOE should be valuable assets for those purposes. Those data will also be useful for determining the sensitivity of the retrievals to the viewing conditions.

4.3.5.4. *Quality Control and Diagnostics*

The initial quality control occurs within the basic algorithms. Constraints are also applied to ensure that no physically unreasonable values are passed to the next subsystem. Particle sizes are not allowed to fall outside of prespecified limits that depend on phase. Cloud temperatures are not allowed to exceed the warmest temperature in the sounding or at the surface, whichever is greatest. Cloud temperatures must be warmer than the tropopause temperature minus 5 K. As a consistency check, the cloud temperatures will also be compared to the values derived for the layer clouds. Liquid water path and optical depths will be capped to prevent unrealistic values. In all cases, a new value, from adjacent pixels or the nearest cloud layer or from a default value set, will replace the suspect pixel value. A quality flag will be set to indicate what bound was violated. A flag will also be set to denote which methodology or replacement technique produced the final cloud property values. Other diagnostics and quality checks will be implemented as needed.

4.3.5.5. *Numerical Computation Considerations*

The code as currently developed processes up to 275 pixels per second on a 300 *Mflop* CPU. While the speed is less than real time, the operational algorithms will perform at higher rates as a result of code optimization.

4.3.6. **References**

- Ackerman, Steven A.; and Stephens, Graeme L. 1987: The Absorption of Solar Radiation by Cloud Droplets—An Application of Anomalous Diffraction Theory. *J. Atmos. Sci.*, vol. 44, pp. 1574–1588.
- Ackerman, Steven A.; Smith, W. L.; Revercomb, H. E.; and Spinhirne, J. D. 1990: The 27–28 October 1986 FIRE IFO Cirrus Case Study—Spectral Properties of Cirrus Clouds in the 8–12 Micron Window. *Mon. Weather Rev.*, vol. 118, pp. 2377–2388.
- Arking, A.; and Childs, J. D. 1985: Retrieval of Cloud Cover Parameters From Multispectral Satellite Images. *J. Climat. & Appl. Meteorol.*, vol. 24, pp. 322–333.
- Baum, Bryan A.; Arduini, Robert F.; Wielicki, Bruce A.; Minnis, Patrick; and Si-Chee, Tsay 1994: Multilevel Cloud Retrieval Using Multispectral HIRS and AVHRR Data: Nighttime Oceanic Analysis. *J. Geophys. Res.*, vol. 99, no. D3, pp. 5499–5514.
- Baum, Bryan A.; Wielicki, Bruce A.; Minnis, Patrick; and Parker, Lindsay 1992: Cloud-Property Retrieval Using Merged HIRS and AVHRR Data. *J. Appl. Meteorol.*, vol. 31, pp. 351–369.
- Blau, H. H., Jr.; Espinola, R. P.; and Reifenstein, E. C., III 1966: Near Infrared Scattering by Sunlit Terrestrial Clouds. *Appl. Opt.*, vol. 5, pp. 555–564.
- Charlson, Robert J.; Warren, Stephen G.; Lovelock, James E.; and Andreae, Meinrat O. 1987: Oceanic Phytoplankton, Atmospheric Sulphur, Cloud Albedo and Climate. *Nature*, vol. 326, pp. 655–661.

- Coakley, James A., Jr.; Bernstein, Robert L.; and Durkee, Philip A. 1987: Effect of Ship-Stack Effluents on Cloud Reflectivity. *Science*, vol. 237, pp. 1020–1022.
- Curran, R. J.; and Wu, M.-L. C. 1982: Skylab Near-Infrared Observations of Clouds Indicating Supercooled Liquid Water Droplets. *J. Atmos. Sci.*, vol. 39, pp. 635–647.
- d'Entremont, Robert P. 1986: Low- and Mid-Level Cloud Analysis Using Nighttime Multispectral Imagery. *J. Climat. & Appl. Meteorol.*, vol. 25, pp. 1853–1869.
- Duda, D. P.; Stephens, G. L.; and Cotton, W. R. 1994: Impact of Enhanced CCN Concentrations on the Radiative Properties of a 3D Marine Stratocumulus Cloud. *Eighth Conference on Atmospheric Radiation*, AMS, pp. 262–264.
- Fu, Qiang; and Liou, K. N. 1992: On the Correlated k -Distribution Method for Radiative Transfer in Nonhomogeneous Atmospheres. *J. Atmos. Sci.* vol. 49, no. 22, pp. 2139–2156.
- Hale, G. M.; and Query, M. R. 1973: Optical Constants of Water in the 200-nm to 200-Micron Wavelength Region. *Appl. Opt.*, vol. 12, pp. 555–563.
- Han, Q. 1992: Global Survey of Effective Particle Size in Liquid Water Clouds. Ph.D. Diss., Columbia University, New York.
- Hansen, J. E.; and Travis, L. D. 1974: Light Scattering in Planetary Atmospheres. *Space Sci. Rev.*, vol. 16, pp. 527–610.
- Hansen, J. E.; and Pollack, J. B. 1970: Near-Infrared Light Scattering by Terrestrial Clouds. *J. Atmos. Sci.*, vol. 27, pp. 265–281.
- Heck, Patrick W.; Mayer, Shalini; Young, David F.; Minnis, Patrick; Takano, Yoshihide; Liou, Kuo-Nan; and Spinhirne, James D. 1993: Comparison of Radiation and Cloud Parameters Derived From Satellite and Aircraft Measurements During FIRE 2 Cirrus IFO. *The FIRE Cirrus Science Results 1993*, David S. McDougal, ed., NASA CP-3238, pp. 24–27.
- Heymsfield, A. J.; and Platt, C. M. R. 1984: A Parameterization of the Particle Size Spectrum of Ice Clouds in Terms of the Ambient Temperature and the Ice Water Content. *J. Atmos. Sci.*, vol. 41, pp. 846–855.
- Hunt, G. E. 1973: Radiative Properties of Terrestrial Clouds at Visible and Infra-Red Thermal Window Wavelengths. *Q. J. R. Meteorol. Soc.*, vol. 99, pp. 346–369.
- Inoue, T. 1985: On the Temperature and Effective Emissivity Determination of Semi-Transparent Cirrus Clouds by Bi-Spectral Measurements in the 10 Micron Window Region. *Meteorol. Soc. Japan*, vol. 63, pp. 88–99.
- King, Michael D.; Kaufman, Yoram J.; Menzel, W. Paul; and Tanre, Didier D. 1992: Remote Sensing of Cloud, Aerosol, and Water Vapor Properties From the Moderate Resolution Imaging Spectrometer (MODIS). *IEEE Trans. Geosci. & Remote Sens.*, vol. 30, pp. 2–27.
- King, M. D.; and Tsay, S. C. 1993: Theoretical Basis of Cloud Retrieval Algorithms for MODIS: Cloud Cover, Thermodynamic Phase, Optical Thickness and Effective Particle Radius. *MODIS Algorithm Theoretical Basis Document*, p. 32.
- Kneizys, F. X.; Shettle, E. P.; Abreu, L. W.; Chetwynd, J. H.; Anderson, G. P.; Gallery, W. O.; Shelby, J. E. A. and Clough, S. A. 1988: *Users Guide to LOWTRAN 7*. AFGL-TR-88-0197, U.S. Air Force. (Available from DTIC as AD A206 773.)
- Kratz, D. P. 1995: The Correlated k -Distribution Technique as Applied to the AVHRR Channels. *J. Quant. Spectrosc. Radiat. Transfer*, vol. 53, pp. 501–507.
- Lin, Xijian; and Coakley, James A., Jr. 1993: Retrieval of Properties for Semitransparent Clouds From Multispectral Infrared Imagery Data. *J. Geophys. Res.*, vol. 98, no. 10, pp. 18,501–18,514.
- Liou, K. 1974: On the Radiative Properties of Cirrus in the Window Region and Their Influence on Remote Sensing of the Atmosphere. *J. Atmos. Sci.*, vol. 31, pp. 522–532.
- Liou, K. N.; Ou, S. C.; Takano, Y.; Valero, F. P. J.; and Ackerman, T. P. 1990a: Remote Sounding of the Tropical Cirrus Cloud Temperature and Optical Depth Using 6.5 and 10.5-Micron Radiometers During STEP. *J. Appl. Meteorol.*, vol. 29, pp. 716–726.
- Liou, K. N.; Takano, Y.; Ou, S. C.; Heymsfield, A.; and Kreiss, W. 1990b: Infrared Transmission through Cirrus Clouds—A Radiative Model for Target Detection. *Appl. Opt.*, vol. 29, pp. 1886–1896.
- Masuda, Kazuhiko; and Takashima, Tsutomu 1990: Deriving Cirrus Information Using the Visible and Near-IR Channels of the Future NOAA-AVHRR Radiometer. *Remote Sens. Environ.*, vol. 31, pp. 65–81.
- Minnis, P.; Young, D. F.; Garber, D. P.; Takano, Y.; and Liou, K. N. 1994: Effects of Cloud Particle Size and Shape on Satellite Remote Sensing of Cloud Properties. *Eighth Conference on Atmospheric Radiation*, AMS, pp. 418–420.

- Minnis, Patrick; Heck, Patrick W.; and Young, David F. 1993a: Inference of Cirrus Cloud Properties Using Satellite-Observed Visible and Infrared Radiances. II—Verification of Theoretical Cirrus Radiative Properties. *J. Atmos. Sci.*, vol. 50, no. 9, pp. 1305–1322.
- Minnis, Patrick; Heck, Patrick W.; Young, David F.; Fairall, C. W.; and Snider, J. B. 1992: Stratocumulus Cloud Properties Derived From Simultaneous Satellite and Island-Based Instrumentation During FIRE. *J. Appl. Meteorol.*, vol. 31, pp. 317–339.
- Minnis, Patrick; Liou, Kuo-Nan; and Takano, Yoshihide 1993b: Inference of Cirrus Cloud Properties Using Satellite-Observed Visible and Infrared Radiances. I—Parameterization of Radiance Fields. *J. Atmos. Sci.*, vol. 50, no. 9, pp. 1279–1304.
- Nakajima, Teruyuki; and King, Michael D. 1990: Determination of the Optical Thickness and Effective Particle Radius of Clouds From Reflected Solar Radiation Measurements. I—Theory. *J. Atmos. Sci.*, vol. 47, pp. 1878–1893.
- Nakajima, Teruyuki; King, Michael D.; Spinhirne, James D.; and Radke, Lawrence F. 1991: Determination of the Optical Thickness and Effective Particle Radius of Clouds From Reflected Solar Radiation Measurements. II—Marine Stratocumulus Observations. *J. Atmos. Sci.*, vol. 48, pp. 728–750.
- Ou, S. C.; Liou, K. N.; Gooch, W. M.; and Takano, Y. 1993: Remote Sensing of Cirrus Cloud Parameters Using Advanced Very-High-Resolution Radiometer 3.7- and 10.9- μm Channels. *Appl. Opt.*, vol. 32, no. 12, pp. 2171–2180.
- Parol, F.; Buriez, J. C.; Brogniez, G.; and Fouquart, Y. 1991: Information Content of AVHRR Channels 4 and 5 With Respect to the Effective Radius of Cirrus Cloud Particles. *J. Appl. Meteorol.*, vol. 30, pp. 973–984.
- Prabhakara, C.; Fraser, R. S.; Dalu, G.; Wu, Man-Li C.; and Curran, R. J. 1988: Thin Cirrus Clouds—Seasonal Distribution Over Oceans Deduced From Nimbus-4 IRIS. *J. Appl. Meteorol.*, vol. 27, pp. 379–399.
- Radke, Lawrence F.; Coakley, James A., Jr.; and King, Michael D. 1989: Direct and Remote Sensing Observations of the Effects of Ships on Clouds. *Science*, vol. 246, pp. 1146–1149.
- Rawlins, F.; and Foot J. S. 1990: Remotely Sensed Measurements of Stratocumulus Properties During FIRE Using the C130 Aircraft Multi-Channel Radiometer. *J. Atmos. Sci.*, vol. 47, pp. 2488–2503.
- Reynolds, D. W.; and Vonder Haar, T. H. 1977: A Bispectral Method for Cloud Parameter Determination. *Mon. Weather Rev.*, vol. 105, pp. 446–457.
- Rossow, William B.; and Lacis, Andrew A. 1990: Global, Seasonal Cloud Variation From Satellite Radiance Measurements. II—Cloud Properties and Radiative Effects. *J. Climat.*, vol. 3, pp. 1204–1253.
- Rossow, William B.; Garder, Leonid, C.; Lu, Pei-Jane; and Walker, Alison 1992: *International Satellite Cloud Climatology Project (ISCCP): Documentation of Cloud Data*. Centel Federal Services Corp., New York.
- Rossow, W. B.; Mosher, F.; Kinsella, E.; Arking, A.; and Harrison, E. 1985: ISCCP Cloud Algorithm Intercomparison. *J. Climat. & Appl. Meteorol.*, vol. 24, Sept. 1985, pp. 877–903.
- Slingo, A. 1989: A GCM Parameterization for the Shortwave Radiative Properties of Water Clouds. *J. Atmos. Sci.*, vol. 46, pp. 1419–1427.
- Smith, William L., Jr.; Minnis, Patrick; Alvarez, Joseph M.; Uttal, Taneil; Intrieri, Janet M.; Ackerman, Thomas P; and Clothiaux, Eugene 1993: Development of Methods for Inferring Cloud Thickness and Cloud Thickness and Cloud-Base Height From Satellite Radiance Data. *The FIRE Cirrus Science Results 1993*, David S. McDougal, ed., NASA CP-3238, pp. 32–35.
- Stackhouse, Paul W., Jr.; and Stephens, Graeme L. 1994: Investigation of the Effects of the Macrophysical and Microphysical Properties of Cirrus Clouds on the Retrieval of Optical Properties—Results for FIRE 2. *The FIRE Cirrus Science Results 1993*, David S. McDougal, ed., NASA CP-3238, pp. 189–192.
- Stamnes, Knut; Tsay, S.-Chee; Jayaweera, Kolf; and Wiscombe, Warren 1988: Numerically Stable Algorithm for Discrete-Ordinate-Method Radiative Transfer in Multiple Scattering and Emitting Layered Media. *Appl. Opt.*, vol. 27, pp. 2502–2509.
- Stephens, G. L. 1978: Radiation Profiles in Extended Water Clouds. Part I—Theory. Part II: Parameterization Schemes. *J. Atmos. Sci.*, vol. 35, pp. 2111–2132.
- Stone, Robert S.; Stephens, Graeme, L.; Platt, C. M. R.; and Banks, S. 1990: The Remote Sensing of Thin Cirrus Cloud Using Satellites, Lidar and Radiative Transfer Theory. *J. Appl. Meteorol.*, vol. 29, pp. 353–366.
- Takano, Yoshihide; and Liou, Kuo-Nan 1989: Solar Radiative Transfer in Cirrus Clouds. I—Single-Scattering and Optical Properties of Hexagonal Ice Crystals. *J. Atmos. Sci.*, vol. 46, pp. 3–36.

- Takano, Y.; Liou, K. N.; and Minnis, P. 1992: The Effects of Small Ice Crystals on Cirrus Infrared Radiative Properties. *J. Atmos. Sci.*, vol. 49, no. 16, pp. 1487–1493.
- Twomey, S. 1977: The Influence of Pollution on the Shortwave Albedo of Clouds. *J. Atmos. Sci.*, vol. 34, pp. 1149–1152.
- Twomey, S.; and Cocks, T. 1982: Spectral Reflectance of Clouds in the Near-Infrared—Comparison of Measurements and Calculations. *J. Meteorol. Soc. Japan*, vol. 60, pp. 583–592.
- Twomey, S.; and Cocks, T. 1989: Remote Sensing of Cloud Parameters From Spectral Reflectance in the Near-Infrared. *Beitr. Phys. Atmos.*, vol. 62, no. 3, pp. 172–179.
- Twomey, S.; and Seton, K. J. 1980: Inferences of Gross Microphysical Properties of Clouds From Spectral Reflectance Measurements. *J. Atmos. Sci.*, vol. 37, pp. 1065–1069.
- Van De Hulst, Hendrik Christoffel 1957: *Light Scattering by Small Particles*. John Wiley & Sons, 1957.
- Wielicki, Bruce A.; Suttles, J. T.; Heymsfield, Andrew J.; Welch, Ronald M.; Spinhirne, James D.; Wu, Man-Li C.; and Starr, David O'C. 1990: The 27-28 October 1986 FIRE IFO Cirrus Case Study—Comparison of Radiative Transfer Theory With Observations by Satellite and Aircraft. *Mon. Weather Rev.*, vol. 118, pp. 2356–2376.
- Wigley T. M. L. 1989: Possible Climate Change Due to SO₂-Derived Cloud Condensation Nuclei. *Nature*, vol. 339, pp. 365–367.
- Wu, Man-Li C. 1987: A Method for Remote Sensing the Emissivity, Fractional Cloud Cover and Cloud Top Temperature of High-Level, Thin Clouds. *J. Climat. & Appl. Meteorol.*, vol. 26, pp. 225–233.
- Young, D. F.; Mayor, S.; Minnis, P.; Intrieri, J. M.; Matrosov, S.; and Snider, J. 1994: Comparison of Satellite and Surface-Based Remote Sensing of Cloud Microphysical Properties During FIRE Cirrus Phase II. *Eighth Conference on Atmospheric Radiation*, AMS, pp. 231–233.
- Young, D. F.; Minnis, P.; Katsaros, K.; Dybbroe, A.; and Mileta, J. 1992: Comparison of Techniques for Deriving Water-Cloud Microphysical Properties From Multiple Satellite Data. *Proceedings of the 11th International Conference Clouds and Precipitation*, pp. 1053–1056.
- Young, D. F.; Minnis, P.; Snider, J. B.; Uttal, T.; Intrieri, J. M.; and Matrosov, S. 1993: Comparison of Cloud Microphysical Parameters Derived From Surface and Satellite Measurements During FIRE Phase II. *Proceedings of the FIRE Cirrus Science Conference*, pp. 52–55.

Appendix

Correction for Gaseous Absorption

Numerous cloud property retrieval techniques require knowledge of the absorption properties of the atmosphere as an integral part of the analysis. Complementary analysis of satellite data with radiative transfer theory improves not only our ability to analyze and understand the data, but our understanding of the physics of the processes modeled. To this end, the absorption by molecular species in the clear-sky pixels is accomplished by means of the correlated k -distribution technique.

Correlated k -Distribution Technique

Various modeling techniques are available to account for the observed absorption of electromagnetic radiation by the molecules which are present in planetary atmospheres. The line-by-line, or monochromatic, procedure is very precise and has an accuracy that is limited only by the extent of our knowledge of the interactions of matter with energy. Such precision, however, is only obtained at the cost of very intensive routines which are not practical in production calculations. To overcome the computational burden of the line-by-line procedure, narrowband and broadband techniques have been devised. While these band models can be made arbitrarily accurate for a homogeneous (constant temperature, pressure, etc.) atmosphere, they require a scaling procedure to account for the inhomogeneity found in realistic atmospheres. In essence, the scaling procedure transforms the inhomogeneous pathlength found in a realistic atmosphere into an equivalent homogeneous pathlength. While entirely satisfactory for the case where only absorption is present, such a transformation is not acceptable for cases where scattering is involved. Nevertheless, a technique, known as the correlated k -distribution, has been devised to accurately and efficiently calculate molecular absorption for a inhomogeneous path without a scaling approximation.

Taking for a moment any arbitrary spectral interval, if the absorption coefficient (k) is plotted against wavenumber ω , a highly nonmonotonic plot will be obtained. The line-by-line procedure resorts to retracing this plot with sufficient spectral resolution so as to accurately reproduce the spectrum of absorption coefficients. An examination of this plot of k versus ω will reveal that similar values of k occur many times. Thus arises the concept of the k distribution. If a transformation of coordinates is made from wavenumber space to cumulative probability space $g(k)$, it will be observed that the highly nonmonotonic plot of k versus ω will become a monotonic plot of k versus $g(k)$. To this point, the only information which has been discarded is the precise spectral location of a particular k ; however, no gain in speed has been obtained. Recall that only the terms of the integration have been reordered. It is noted, however, that the monotonic distribution of k versus $g(k)$ can have far fewer (often 3 to 5 orders of magnitude) terms, yet retain very high accuracy for the calculation of the absorption for the specified spectral interval. This reduction in the number k values needed leads to the increased efficiency necessary for any production calculations. To account for a inhomogeneous path, an additional assumption is required. Given any pressure or temperature encountered in the atmosphere, it is assumed that any particular absorption coefficient will always have the same cumulative probability. Thus, the location in cumulative probability space of any absorption coefficient at any given pressure or temperature will be correlated with that of the absorption coefficient at a specified reference pressure and temperature. This leads to the concept of the correlated k -distribution. Fu and Liou (1992) have demonstrated conclusively that the assumption of correlation is sufficiently accurate for most purposes. Since the k 's are assumed to be correlated for any pressure and temperature, the correlated k -distribution procedure can be calculated through an inhomogeneous atmosphere in the same manner as a monochromatic calculation. Thus, the correlated k -distribution allows for an efficient and accurate calculation which is compatible with most scattering routines.